The University of Osaka
Institutional Knowledge Archive

Title	Low temperature sintering mechanism and designing silver sinter paste for die-attach of Wide Band Gap semiconductor
Author(s)	廉, 済胤
Citation	大阪大学, 2020, 博士論文
Version Type	VoR
URL	https://doi.org/10.18910/76531
rights	
Note	

The University of Osaka Institutional Knowledge Archive : OUKA

https://ir.library.osaka-u.ac.jp/

The University of Osaka

Doctoral Dissertation

Low temperature sintering mechanism and designing silver sinter paste for die-attach of wide band gap semiconductor

Jeyun Yeom

January 2020

Department of Adaptive Machine Systems
Graduate school of Engineering
Osaka University

Supervisor Prof. Suganuma Katsuaki, Ph. D.

The Institute of Scientific and Industrial Research

Osaka University

Doctoral Committee

Prof. Suganuma Katsuaki, Ph. D.

The Institute of Scientific and Industrial Research

Osaka University

Prof. Yuichiro Koizumi, Ph. D.

Division of Materials and Manufacturing Science,

Graduate School of Engineering,

Osaka University

Assoc. Prof. Shijo Nagao, Ph. D.

The Institute of Scientific and Industrial Research

Osaka University

Assoc. Prof. Tohru Sugahara, Ph. D.

The Institute of Scientific and Industrial Research

Osaka University

Low temperature sintering mechanism and designing silver sinter paste for die-attach of wide band gap semiconductor

Abstract

The purpose of the study is to understand previously reported fast and sound bonding (~ 40 MPa) achieved by Ag sinter pastes and develop new sinter paste for realizing high temperature endurable die-attachment. The dissertation dealt with the interaction between chemically synthesized Ag particles and solvent, and developing *in situ* chemical synthesis sinter paste using redox reaction. The unique sintering mechanism of Ag flakes *in situ* formed Ag nanoparticles is discussed.

In Chapter 1, the background of die-attach materials for realizing high temperature semiconductor packaging is explained. One of most promising candidates is Ag sinter paste due to its excellent bonding strength with low bonding temperature and pressure. It provides high reliability and high anti-oxidation. There are some challenging points in Ag sintering. Ag nanoparticles need organics additives for storage, which leads to inhibit sintering. The price of Ag nanoparticles is ten times higher than micron-sized Ag particles, and it restrict the application of nano-silver paste in industry. Micron-sized Ag pastes has low packing density and surface energy, which increases the sintering temperature and pressure, and cannot lead to successful high temperature packaging due to weak bonding. Therefore, analysis on new Ag sinter bonding mechanism and designing sinter paste are needed.

In Chapter 2, the sintering mechanism of polyol-synthesized submicron and micron Ag paste is mainly discussed. The Ag pastes exhibited sound bonding (~ 40 MPa) though, sintering condition is at 200 °C, 0.4 MPa, which is not expected owing to low surface energy. To understand the mechanism, we compared it with hybrid Ag particles consisting of micron-sized Ag fakes and submicron-sized Ag particles. During the sintering process, *in situ* formed Ag nanoparticles (Ag NPs) were observed only in Ag tracks derived from polyol-synthesized Ag paste sintered at 175 °C, and they are considered to be the main driving force for particle sintering. The main factor for Ag NPs formation is the residual Ag ions, which can realize low temperature sintering.

In Chapter 3, a unique mechanism in Ag micro flake sintering which reveals that self-produced Ag nanoparticles, created by the heating of the sintering process, is discussed. The flakes have microstrain due to the higher dislocation density of the crystalline structure. The release of microstrain in the flake particles during heating leads to the production of Ag nanoparticles, which is a significant driving force in the sintering process.

In Chapter 4, improving the sintering performance of micron Ag pastes via *in situ* polyol synthesis is presented. The chemically modified Ag pastes exhibited higher bonding strength and electrical conductivity than their corresponding non-chemically modified Ag pastes. The chemical modification is expected to achieve pure metallic bonding with increased sintering performance.

In Chapter 5, the summary of the dissertation is presented.

The dissertation presented the unique factors of Ag sintering rather than the main driving force of sintering such as surface energy. The unique characteristic of synthesized Ag particle paste and micro-strained Ag particle paste exhibited *in situ* formation Ag NPs, without using organic additives for conservation. The mechanism and designing Ag pastes are believed to give ways realizing high temperature and high reliable packaging.

Contents

List of Figures

List of Tables

This page is left blank intentionally.

Chapter 1

Introduction

1.1 Development and challenge of next generation power devices

1.1.1 Global issues on energy and needs for power device

Nowadays, with increasing demand on solving global issues related to energy such as fossil fuels depletion, carbon dioxide (CO_2) emissions, much effort has been put on developing green and sustainable energy such as fuel cells, photovoltaic, wind power, and etc. Once we have established new energy source, there is another serious issue that large amount of energy is consumed during energy conversion, distribution, storage. Power electronics plays a key role in the conversion AC - DC, DC – DC, and distribution of electrical energy [1]. Thus, power electronics is one of the essential devices for efficient usage of electric energy, which governs entire process from generation, transmission, and consumption.

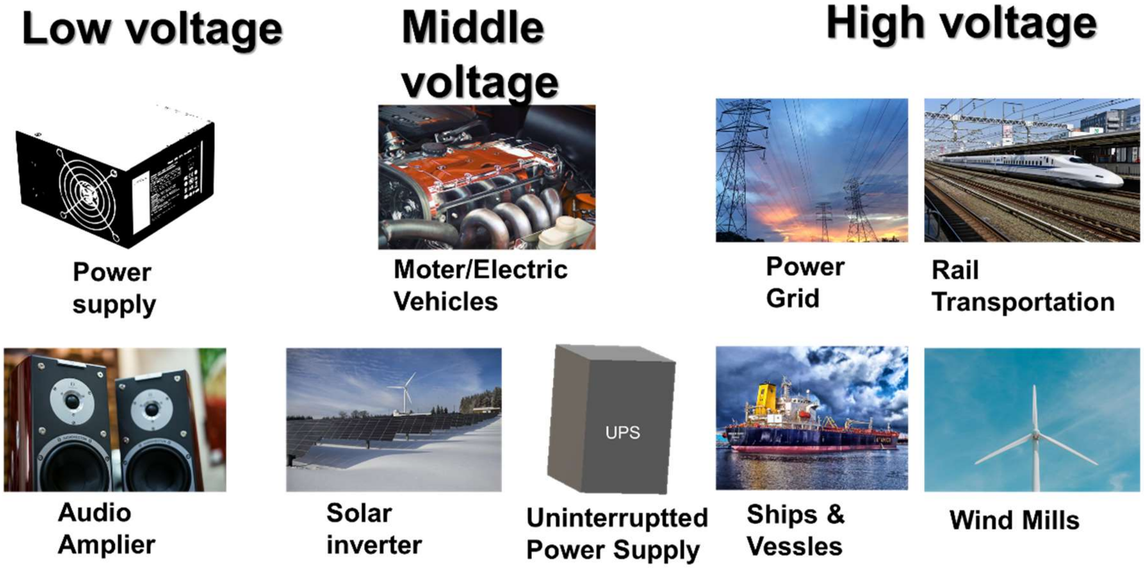

Fig. 1. 1 Schematic diagram of power device applications.

Fig. 1.1 shows a schematic diagram of its use in industrial, commercial, electrical railways, UPS. With the growing usage of power devises, the energy efficiency of conversion, storage, is highly needed.

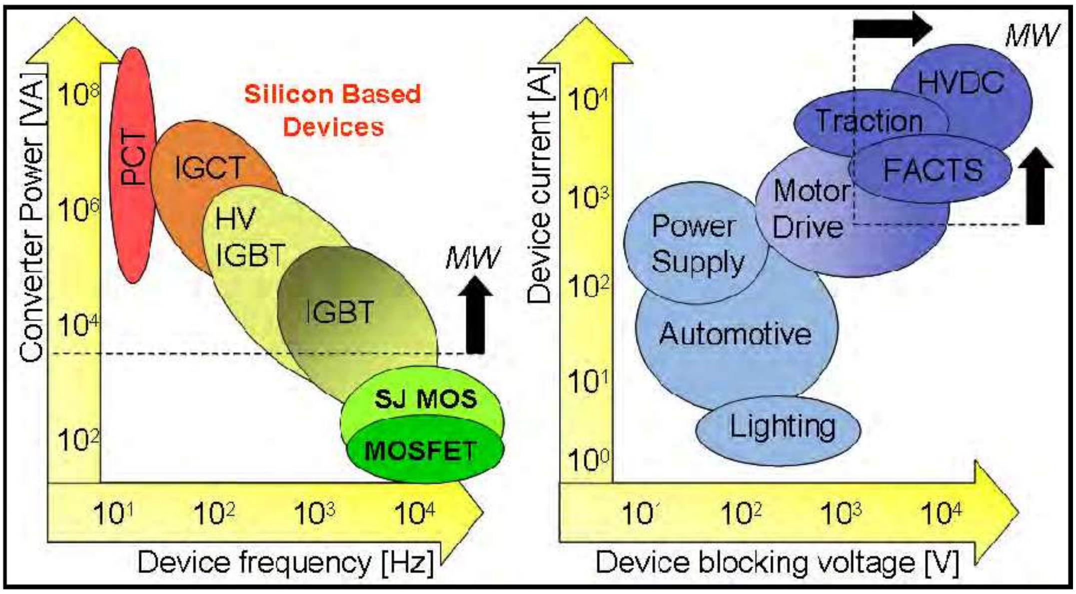

Fig. 1. 2 Characteristic of power devices and their application areas [2]. Copyright 2009, IEEE.

1.1.2 History of power devices

As power electronics applied to wide range of areas, conversion power ranges from a few VA to 10 MVA, and operation frequency ranges from a few Hz to MHz. One power device cannot cover this wide range of voltage and of frequency, which resulting in various power devices in the market. Fig. 1.2 shows characteristic of power devices and their application areas.

At the beginning, bipolar transistor power device was made with Germanium (Ge) crystal. However, it has a narrow bandgap of 0.7 eV and low operating temperature (< 90 °C) [3,4]. Ge was replaced with Silicon (Si) in the 1950s, which has better material characteristic such as higher bandgap 1.1 eV and operating temperature (< 150 °C) [5]. By the progress of fabrication of high-quality Si single crystal growth, structure improvement, and packaging technology improvement, Si device got increased operation voltage and current. In the mainstream of power devices, Si semiconductors mainly played main role until now.

Various Si power devices were introduced during the last half century. The power devices other than bipolar transistor were developed including thyristor, power Metal-Oxide-Semiconductor, and Field-Effect Transistor (MOSFET). Bipolar transistor operates using both electrons and holes as charge carriers, and can be used as amplifiers or switches. Thyristors consists of three PN-junctions, which were first introduced in the 1950s. At the initial stage, the current and voltages is limited to 100 A and several hundred, respectively. Thyristors have wide application area such as motor drives, high power inverter and traction, and high-voltage direct current (HVDC) transmission networks.

Since the operating frequency of bipolar transistor and thyristors was limited, power MOSFET was introduced in the 1970s, and could overcome the power limit problem. Power MOSFET is unipolar type transistor using only electron as its carrier, which leads to 10 times higher frequency than bipolar transistor. However, power MOSFET is vulnerable to high operating voltage and current due to its structure. To solve this issue, the various types of Si power devices has been developed for high current and high-speed switching. Still, high voltage operation and high-speed switching has not been realized with bipolar transistor and power MOSFET. Fig. 1.2 shows the operation frequencies of power device semiconductor. The advantage of high operation current and voltage and frequency was realized by IGBT (Insulated Gate Bipolar Transistor), which was introduced in 1980s. Thyristors, GTO (Gate Turn-Off thyristor) were also developed.

1.2 Advent of Wide Band Gap (WBG) power device

1.2.1 Limitation of Si devices

Until now, Silicon technology has been widely used for power devices, and will continue to govern the power device market for a while. There are rooms to ameliorate the efficiency of Si device by introducing better packaging, Si wafer technology, changing the structure of devices. However, the conversion efficiency of Si devices is reaching to their theoretical maximum value due to limitation of Si material properties. Also, the junction temperature of the devices is restricted to 150-200 °C [6]. Therefore, the devices cannot operate over 200 °C without heavy cooling system. The complex cooling system also includes connector and wires, even more weight and volume to the device, which may lead to failure risk. In some area such as the electronic vehicle, down-hole oil, gas industries for well logging, electric aircraft, renewable energy power devices with increased operating temperature, high reliability are highly required [7].

Table 1.1 Material characteristics of various semiconductors [5].

Property	Si	GaAs	6H-SiC	4H-SiC	GaN	Diamond
Bandgap, E_g (eV)	1.12	1.43	3.03	3.26	3.45	5.45
Dielectric constant, ε_r[1]	11.9	13.1	9.66	10.1	9	5.5
Electric Breakdown Field, E_c (kV/cm)	300	400	2500	2200	2000	10000
Electron Mobility, μ_n ($cm^2/V \cdot s$)	1500	8500	500 80	1000	1250	2200
Hole Mobility, μ_p ($cm^2/V \cdot s$)	600	400	101	115	850	850
Thermal Conductivity, λ (W/cm·K)	1.5	0.46	4.9	4.9	1.3	22
Saturated Electron Drift Velocity, v_{sat} ($\times 10^7$ cm/s)	1	1	2	2	2.2	2.7

[1] $\varepsilon = \varepsilon_r \cdot \varepsilon_o$ where $\varepsilon_0 = 8.85 \times 10^{-12}$ F/m

1.2.2 Wide Band Gap semiconductor

As mentioned above, the limitation of Si material was the problems of high operating temperature, and the conversion energy loss. The problem can be overcome by introducing wide band gap material such as Silicon Carbide (SiC), Gallium Nitride GaN, diamond. Table 1.1 shows material characteristics of various semiconductors. The breakdown field of SiC and GaN is 10 order higher than Si, which allows WBG semiconductor to operate at higher voltages and to have 1/10 thinner drift layer. (see Fig. 1.3) Thin drift layer reduces ohmic resistance, which leads to save the unnecessary thermal energy transformation. Moreover, the faster saturated electron drift velocity they have, the higher operation frequency is allowed. WBG semiconductors also exhibit higher bandgap, and better thermal conductivity (Table 1.1). These properties allow WBG power devices to operate at higher operating junction temperature with high reliability. (see Fig. 1.4)

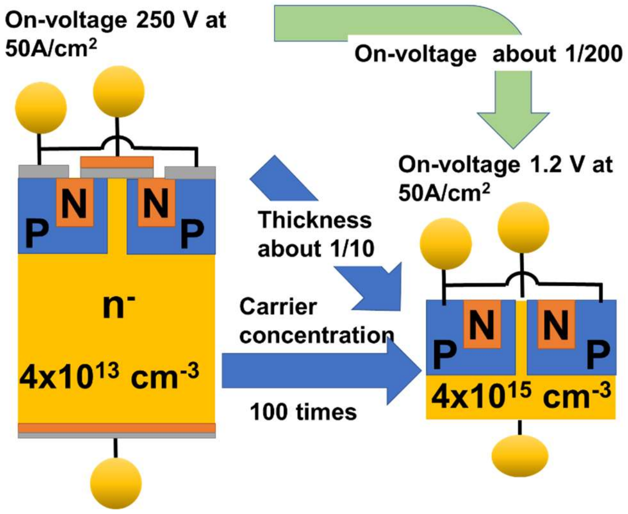

Fig. 1.3 Schematic diagram of comparison between Si and SiC MOSFET.

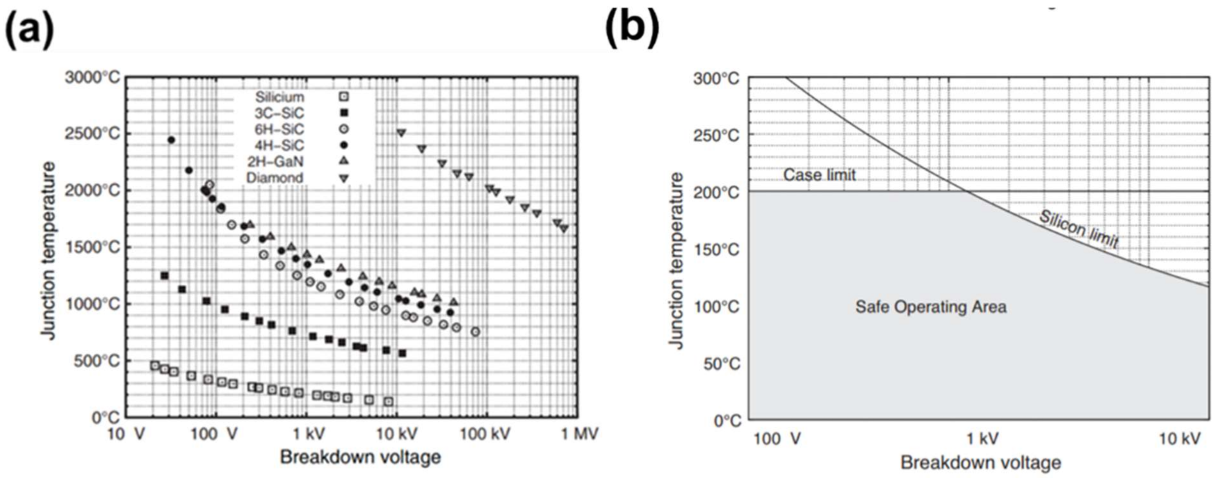

Fig. 1.4 (a) Theoretical operation limits of Si, SiC, GaN and diamond semiconductor (simulation) (b) the operating temperature of Si semiconductor, where the case limit corresponds to a standard package. Reprinted with permission from [8]. Copyright 2011, Elsevier.

As mentioned above, by adopting WBG devices, mass and volume reduction can be achieved. Fig. 1.4 shows WBG semiconductor can operate at high-voltage (> 10kV) and their available junction temperature is over 500 °C. This clearly indicates benefits of WBG power device compared to traditional power Si devices.

1.2.3 Failure of WBG power device and requirement of advanced die-attach materials

To ensure the high reliability of power modules at high operating temperature, packaging become main issue. Fig. 1.5 shows schematic diagram of power module. A module consists of a heat sink, a substrate, terminal leads and WBG die, wire, die-attach and substrate attach. The reported failure mode of power module mainly comes from die attach, wire, and substrate detachment.

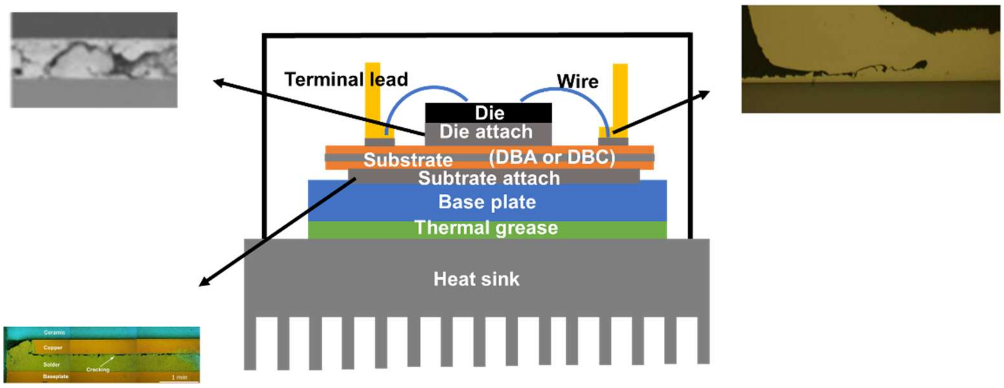

Fig. 1.5 Structure of power module and common failure in packaging [9–11]. Inset figure of Die-attach and wire failures: Copyright 2007, IEEE. Copyright 2018, IEEE.

In this dissertation, our main concern focused on die-attach part, which is one of the main issues of packaging. One of the failure mechanisms of die-attachment is known to be caused by large mismatch in coefficients of thermal expansion (CTE) between die and substrate [12,13]. Due to harsh operation condition, junction temperature will change severely. Therefore, large CTE mismatch causes a large stress gradient and contributes to generation and propagation of crack or void in die-attach. Table 1.2 shows mechanical properties of semiconductor, die-attach materials and substrate.

Table 1. 2 Mechanical properties of semiconductor, die-attach materials and substrates [14–17].

Component	Materials	Coefficient of thermal expansion (ppm/K)	Thermal conductivity ($Wcm^{-1}K^{-1}$)	Young module (GPa)
Die	Si	2.6	1.5	150
	SiC	3.8	5.0	410
	GaN	6.2	1.3	320
Bonding layer	Pb-5Sn	29	0.35	20
	Sn-3Ag-0.5Cu	24	0.59	51
	Sintered Ag	1.9	2.4	9
	Cu_3Sn	19	0.7	108
DBA/DBC substrate	Al	17	2.05	68
	Cu	16.5	4.0	110
	Al_2O_3	6.5	0.3	310
	AlN	4.5	2.9	310
	Si_3N_4	2.6	0.9	314

The large difference in coefficients of thermal expansion between semiconductor and substrates would induce serious damage. Therefore, the structure of ideal device should consider the following requirements: sound bonding that can endure large temperature difference during the thermal cycles. And it should have high thermal conductivity which can deal with heat from operation, which leads to decrease in internal stress based on high temperature. Additionally, IMC (Inter Metallic Compound) layer should not be created during operation, since the brittle nature of IMC is known to induce crack initiation and propagation, and void formation [13].

1.3 Overview of high-temperature die-attach materials and methods

The Pb based-solders, 85-95wt.% of Pb, have been generally used for high temperature die-attach. The melting temperature of Pb–5Sn, Pb–10Sn are about 308-312 ℃ and 275-302 ℃, respectively. The temperature range is apt to high temperature usage of power device, however, with the increasing environmental concerns it is expected that in the future the usage of Pb-based solder will be prohibited by the restriction of hazardous substances (RoHS). Therefore, some candidates for high temperature die-attach materials and methods are introduced. For examples, including Pb-free solders, transient liquid phase (TLP) bonding, Cu sinter bonding, Ag stress-migration bonding (SMB) and Ag sinter bonding method.

1.3.1 Pb-free solders

The Pb-free solders include Au-based solders such as Au-Sn [18,19], Au-Ge [20,21] and Zn-based solders such as Zn-Al [22–24], Zn-Sn [25], and Bi-Ag[26] and Sn-Sb [27]. The Pb free solder and their solidus and liquidus temperature are listed in Table 1.3.

Au-Sn alloys are one of the most promising high temperature Pb-free solders due to their excellent properties such as high yield strength and good wettability, low viscosity, high thermal conductivity (57 W m^{-1} K^{-1}), good electrical properties and excellent corrosion resistance [18,19]. The melting point of Au-20Sn solder is 280 °C and soldering process is performed around 300 °C [18]. Au-Ge solders exhibited high strength and reliability, however, its high soldering process temperature (350 °C) is problem [20]. The high cost of Au-based solders hindered their wide-spreading. High temperature solders, Zn-Al, Zn-Sn, Bi-Ag and Sn-Sb are also one of candidates. Though Zn-based alloys (Zn-Al, Zn-Sn) exhibited excellent thermal conductivity and reliability, they are vulnerable to oxidation, and high melting temperature (380 °C) is flaw [22–25]. Sn-Sb alloy has good creep property and a good reliability; however, they are toxic. Bi-based solders have a low thermal conductivity and poor wettability.

Table 1. 3 Pb free solder and their solidus and liquidus temperature. Reprinted with permission from [28]. Copyright 2009, TMS.

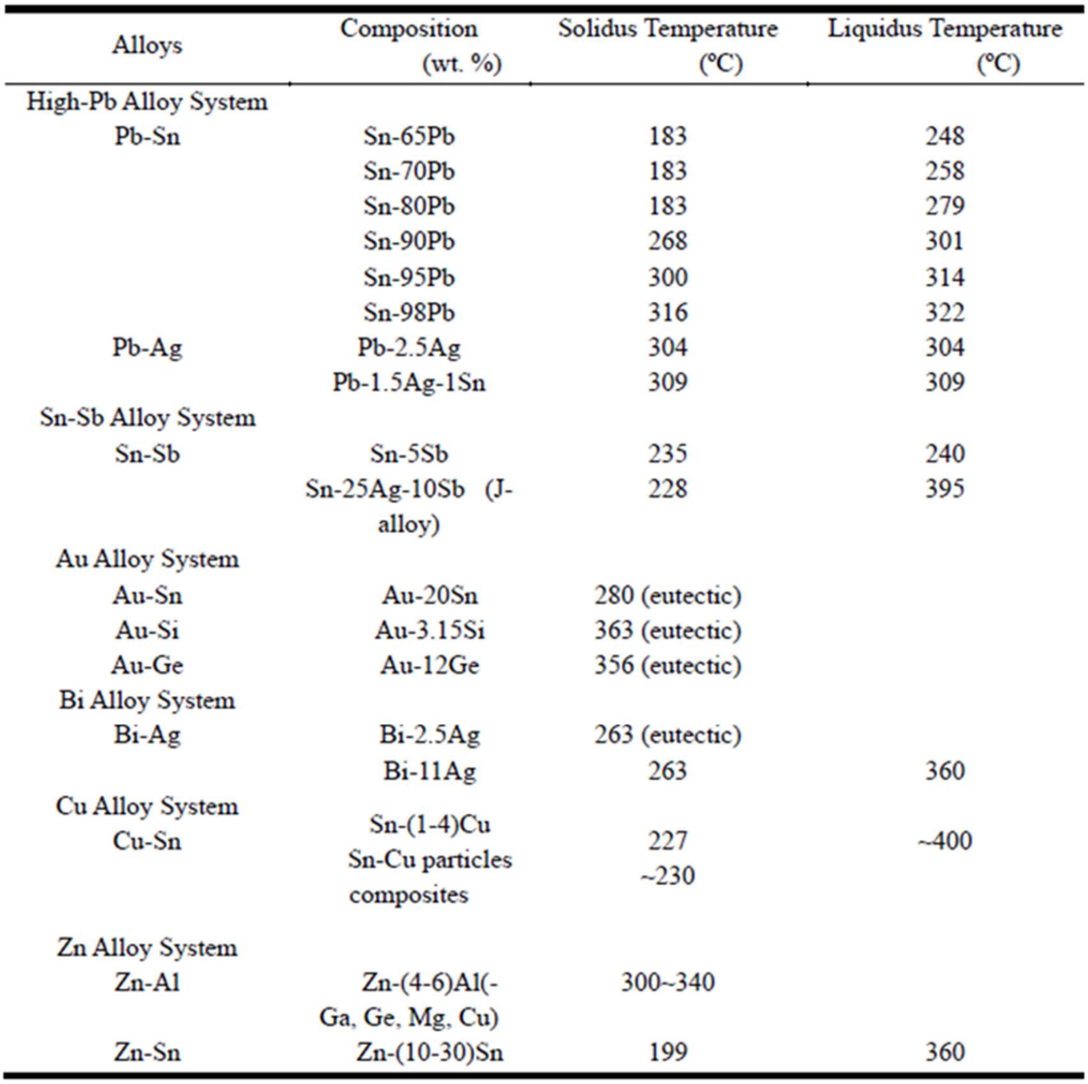

Alloys	Composition (wt. %)	Solidus Temperature (°C)	Liquidus Temperature (°C)
High-Pb Alloy System			
Pb-Sn	Sn-65Pb	183	248
	Sn-70Pb	183	258
	Sn-80Pb	183	279
	Sn-90Pb	268	301
	Sn-95Pb	300	314
	Sn-98Pb	316	322
Pb-Ag	Pb-2.5Ag	304	304
	Pb-1.5Ag-1Sn	309	309
Sn-Sb Alloy System			
Sn-Sb	Sn-5Sb	235	240
	Sn-25Ag-10Sb (J-alloy)	228	395
Au Alloy System			
Au-Sn	Au-20Sn	280 (eutectic)	
Au-Si	Au-3.15Si	363 (eutectic)	
Au-Ge	Au-12Ge	356 (eutectic)	
Bi Alloy System			
Bi-Ag	Bi-2.5Ag	263 (eutectic)	
	Bi-11Ag	263	360
Cu Alloy System			
Cu-Sn	Sn-(1-4)Cu	227	~400
	Sn-Cu particles composites	~230	
Zn Alloy System			
Zn-Al	Zn-(4-6)Al(-Ga, Ge, Mg, Cu)	300~340	
Zn-Sn	Zn-(10-30)Sn	199	360

Table 1.4 Pb-free high temperature solders and their advantages and disadvantages. Reprinted with permission from [29]. Copyright 2012, Elsevier.

Alloy system	Advantages	Disadvantages
Au-Sn	• fluxless • good creep resistance	• expensive • Brittle Au-Sn IMCs
Au-Ge	• low elastic modulus • stable microstructure • relative high strength	• expensive • difficult to manufacture
Bi-Ag	• acceptable melting point • affordable cost	• poor workability • low conductivity
Zn-Al	• low cost • no IMC formed under equilibrium	• highly corrosive • poor wetting
Zn-Sn	• low cost • no IMC formed under equilibrium • ductility improved compared to Zn-Al	• highly corrosive • formation of liquid phase at 199 °C
Sn-Sb	• stable microstructure • good creep properties	• toxic

1.3.2 Transient liquid phase bonding process

Transient liquid phase bonding process (TLP) bonding is often used for high-temperature bonding. TLP is achieved by two kinds of metals, with thin low-melting temperature interlayer metal and high-melting point material. Firstly, the interlayer of low-melting temperature materials melts, then the materials diffuses into the high-melting point material, thereby causing a change of composition at the bond interface with lower melting temperature than parent materials. At isothermal process, solidification is achieved with the diffusion of liquid interlayer away from eutectic point. The schematic diagram of TLP is shown in Fig. 1.6.

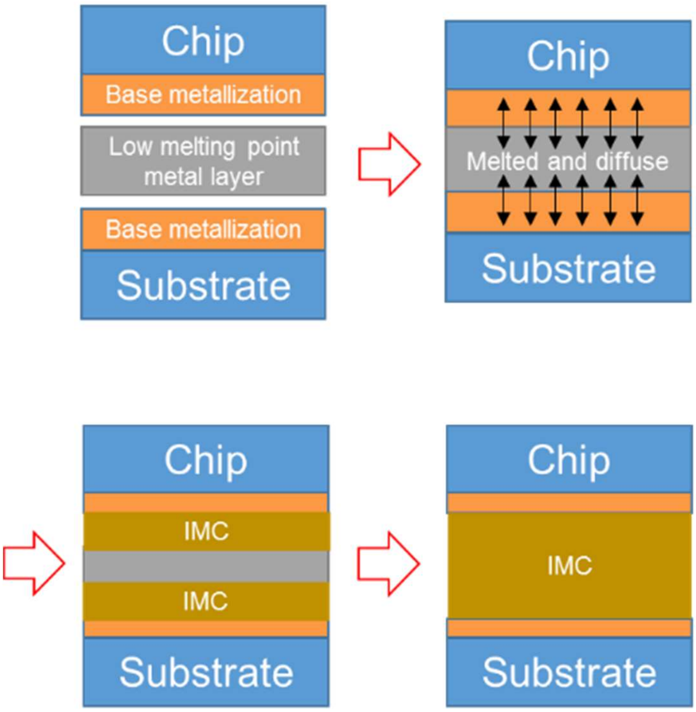

Fig. 1. 6 Schematic diagram of TLP process.

The advantages of TLP bonding technique are high temperature sustainability, cost and moderate bonding pressure/temperature. However, TLP process needs long time to achieve even IMC layer formation. And IMC layers are brittle which leads to crack formation.

1.3.3 Cu sinter paste bonding

Sinter bonding with Cu paste is an excellent candidate for reliable die-attach methods. The thermal conductivity of Cu is similar to that of Ag which has highest conductivity in the metal, while the cost of Cu is much cheaper than that of Ag. Cu is also resistant to electrochemical migration, while Ag is vulnerable to the migration. The only disadvantage of Cu sinter paste bonding seems that Cu particle is prone to oxidation, which make the sintering process is difficult. Under a certain oxygen partial pressure, the diffusion coefficient of Ag become higher, which make Ag sintering without certain gas atmosphere. However, Cu needs protective gas atmosphere, or sometimes even poisonous gas is used such as formic acid.

1.3.4 Ag-Ag direct bonding

Ag-Ag direct bonding is achieved by Ag hillock growth. Oh et al [30–33] reported that Ag hillock growth between two Si substrate with heating realized Ag-Ag direct bonding. (see Fig. 1.7) Hillock growth is related to the relaxation of residual stress, which is induced on thin metallic film by CTE mismatch between film layers [30].

Ag hillock formation is generally known to be directly related to residual stress through creep mechanism [36,37]. Further study clarified that self-produced Ag nanoparticle grow to Ag hillock [35]. Fig. 8 shows that sputtered Ag on Si or after polishing generate Ag nanoparticles (Ag NPs), and grow to Ag hillocks. The formation of Ag NPs and hillock growth mechanism is also supported by nano volcanic eruption theory which explains the role of oxygen and strain [35]. (see Fig. 1. 14) Lin et al maintained that Ag absorbs oxygen along its grain boundary and forms Ag oxides, and under compressive residual stress Ag-O liquid come out to surface and then decomposes to metallic Ag [35]. These founding is also applicable to bulk Ag [34], sputtered Ag film [32,35] and Ag sintered structure[38]. The formation of hillocks from both side of Ag film can produce bonding layer without porosity exhibiting high bonding strength. In addition, the pure Ag layer does not produce IMC, having excellent thermal conductivity for next generation die-attachment.

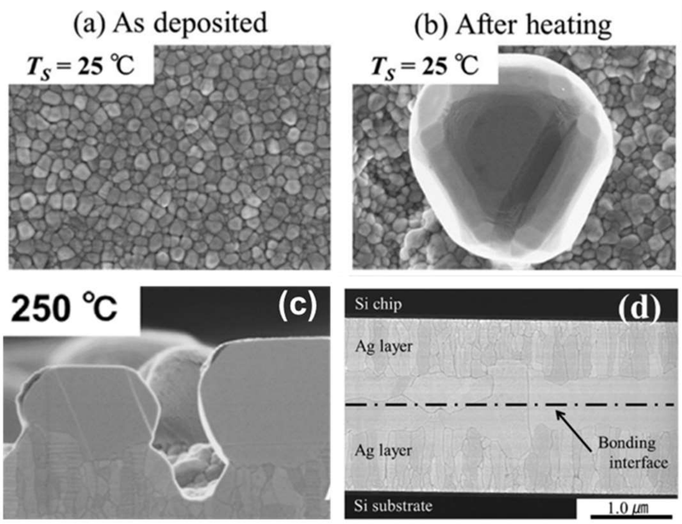

Fig. 1. 7 The sputtered Ag on Si substrate at initial state (a) and after heating process (b). (c) cross-sectional SEM micrograph of hillock growth on Ag films, and (d) Ag-Ag direct bonding achieved by Ag hillock growth. Reprinted with permission from [30,33]. Copyright 2014, AIP publishing. Copyright 2014, Elseiver.

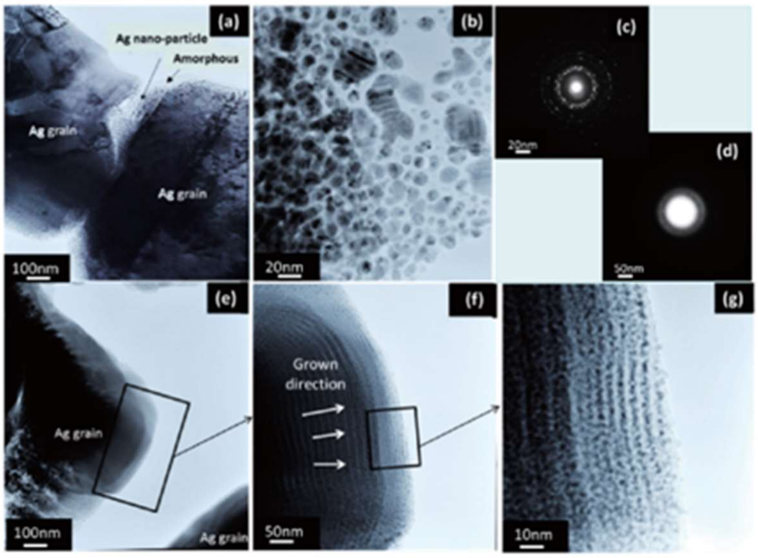

Fig. 1. 8 TEM image of the Si=Ag=Ag=Si structure after annealing at 250 °C for 1 h in air (a); an amplified view of local area between the two Ag grains (b); SAED pattern of AgNPs (c) and the amorphous structure (d); AgNPs grown on the surface of Ag grains in a specific direction (e); and amplified view of the local area (f) and (g). Reprinted with permission from [34]. Copyright 2018, The Japan Society of Applied Physics.

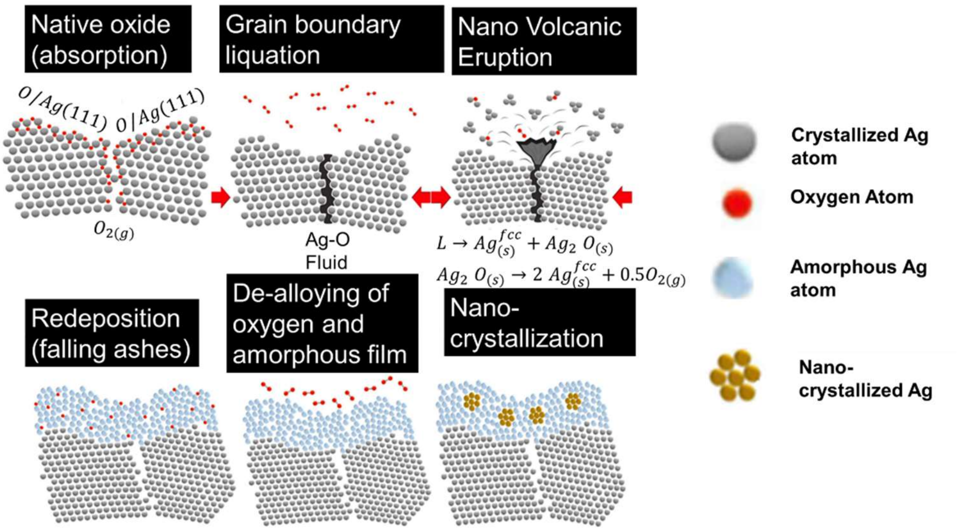

Fig. 1. 9 Schematic diagram of Ag nano-volcanic eruption [35]. The figure is modified from its original version [35].

1.3.5 Ag sinter paste bonding

Pure metal bonding layer is best option for die-attach material since it has high thermal conductivity and ductility. As aforementioned, Ag has highest thermal/electrical conductivity among metals, which make Ag bonding layer attractive. Ag sinter joining generally achieved at 180-300 °C in air without assisting high pressure resulting in pure Ag micro-porous layer without any IMC layer. Recent studies which compared Pb-based solder and Ag sinter methods showed that Ag sinter bonding exhibited much better reliability compared to Pb-based solder. Thus, Ag sinter paste bonding is one of attractive methods for high temperature die-attach methods.

For realizing Ag joint, Ag particles are generally mixed with organic solvent to prepare for Ag paste. A recent study on solvent showed that the choice of solvent extremely changed the sintering performance of Ag pastes: microstructure and shear strength at low temperature of 200 °C [39]. The size of Ag particles is highly related to the sintering performance since the driving force of sintering depends on the surface free energy. For example, Ag nanoparticles sintered even at room temperature showing the electrical resistivity decreased to about 10^{-5} Ω·cm. However, the usage of Ag nanoparticles is restricted owing to their high cost. The cost of Ag nanoparticles is 10 times expensive than that of Ag micron particles. The affordable micron Ag particles sintering is attractive, but they have low surface free energy, which make the sintering condition harsh. The temperature and pressure needed for sintering of Ag micron particles are more than 300 °C, 9 MPa, respectively [40]. Especially high pressure may cause serious damage on substrate during bonding stage, new approach is needed.

The reaction between Ag oxide and solvent with hydroxyl group can decrease the reduction temperature of Ag oxide from 430 °C to 180 °C, and Ag oxide paste is studied [41,42]. However, bonding temperature and pressure is still high, and the shear strength is about 15 MPa. The author's laboratory introduced Ag micron particles and successfully sintered it at 200 °C, 0.4 MPa [43]. The bonding strength was about 40 MPa, which is applicable to next generation power semiconductor. Also, Jiu et al. introduced micron and submicron Ag particle with polyol synthesis and realized the high shear strength over 40 MPa at 200 °C, 0.4 MPa [44]. The results of Ag sinter paste are summarized in Table 1.5.

Table 1. 5 Recent strength results of the sintered Ag joints and their sintering conditions

Size (nm)	**Bonding substrate**	**Temp (^oC)**	**Pressure (MPa)**	**Shear strength (MPa)**	**Ref**
20	Cu plates	150, 200	0	12-30	[45]
40	Cu wire to Cu foil	300	5	21.9	[46]
40,90	Ag-coated Cu plates	250	5	26,50	[47]
5,10, several hundreds	Cu discs	240	40	Over 20 except 10 nm paste	[48]
Commercial paste	Si to Direct Bonding Copper (Ag plated)	240	40	50	[49]
20-168	Ag-coated Cu plates	350	5	13.7	[50]
40	Cu plates	250	20	84	[51]
3000	ENIG-coated Cu discs	200	10	25	[52]
8000	Ag-coated SiC to DBC	300	0.4	>30	[53]
8000,300 (9:1)	Ag-coated SiC to DBC	200, 300	0.4	<40	[43],[54]
8000,3000 (9:1)	Ag-coated SiC to DBC	180	0	42	[40]
8000,600 (98:2)	Ag-coated Cu plates	250	0.4	35	[55]
2500, 400	Ag-coated Cu plate	200	0.4	>40	[44]

Table 1. 6 Summary of various die-attach materials

	Advantages	Disadvantages
Lead-free solder	-acceptable price	-poor reliability -brittle layer based on IMC -high reflow temperature
TLP bonding	-high bonding strength -high thermal reliability -acceptable price	-long bonding time -poor thermal/electrical conductivity - high brittleness
Cu particles sinter joining	-high thermal conductivity -high bonding strength -acceptable price	-oxidation -high temperature, high pressure -protective atmosphere
Ag migration bonding	-nearly perfect bonding layer -good thermal and fatigue reliability -superior thermal conductivity	-complicated manufacturing process -high price
Ag particles sinter joining	-high thermal conductivity -high bonding strength -good thermal reliability -resistant to oxidation	-high price -electrochemical migration

1.4 Purpose and scope of the present study

The purpose of the study is to understand previously reported fast and sound bonding (~ 40 MPa) achieved by Ag sinter pastes, and develop new sinter paste for realizing high temperature endurable die-attachment. The dissertation dealt with the interaction between chemically synthesized Ag particles and solvent, and developing *in situ* chemical synthesis sinter paste using redox reaction. The unique sintering mechanism of Ag flakes, i.e. *in situ* formed Ag nanoparticles is discussed.

In Chapter 1, the background of die-attach materials for realizing high temperature semiconductor packaging is explained. One of most promising candidates is Ag sinter paste due to its excellent bonding strength with low bonding temperature and pressure. It provides high reliability and high anti-oxidation. There are some challenging points in Ag sintering. Nano-sized Ag pastes has organics additives for conservation of Ag particles, micron-sized Ag pastes has low packing density and surface energy, which increases the sintering temperature and pressure and cannot lead to successful high temperature packaging due to weak bonding. Therefore, analysis on new Ag sinter bonding mechanism and designing sinter paste are needed.

In Chapter 2, the sintering mechanism of polyol-synthesized submicron and micron Ag paste is mainly discussed. The Ag pastes exhibited sound bonding (> 40 MPa) though, sintering condition is at 200 °C, 0.4 MPa, which is not expected owing to low surface energy. To understand the mechanism, we compared it with hybrid Ag particles consisting of micron-sized Ag fakes and submicron-sized Ag particles. During the sintering process, *in situ* formed Ag nanoparticles were observed only in Ag tracks derived from polyol-synthesized Ag paste sintered at 175 °C, and they are considered to be the main driving force for particle sintering. The main factor for Ag NPs formation is the residual Ag ions, which can realize low temperature sintering.

In Chapter 3, a unique mechanism in Ag micro flake sintering which reveals that self-produced Ag nanoparticles, created by the heating of the sintering process, is discussed. The flakes have microstrain due to the higher dislocation density of the crystalline structure. The release of microstrain in the flake particles during heating leads to the production of Ag nanoparticles, which is a significant driving force in the sintering process.

In Chapter 4, the improvement of the sintering performance of micron Ag pastes via *in situ* polyol synthesis is presented. The chemically modified Ag pastes exhibited higher bonding strength and electrical conductivity than their corresponding non-chemically modified Ag pastes. The chemical modification is expected to achieve pure metallic bonding with increased sintering performance.

In Chapter 5, the summary of the dissertation is presented.

Reference

[1] J. Millán, A review of WBG power semiconductor devices, in: Proc. Int. Semicond. Conf. CAS, IEEE, 2012: pp. 57–66.

[2] M. Rahimo, S. Klaka, High Voltage Semiconductor Technologies, in: 2009 13th Eur. Conf. Power Electron. Appl., 2009.

[3] D.A. Lapiano-Smith, E.A. Eklund, F.J. Himpsel, L.J. Terminello, Epitaxy of LiF on Ge(100), Appl. Phys. Lett. 59 (1991) 2174–2176.

[4] William F. Waller, Rectifier Circuits, 1972.

[5] J.L. Hudgins, G.S. Simin, E. Santi, M.A. Khan, An assessment of wide bandgap semiconductors for power devices, IEEE Trans. Power Electron. 18 (2003) 907–914.

[6] R.L. Greenwell, B.M. Mccue, L.M. Tolbert, B.J. Blalock, S.K. Islam, High-Temperature SOI-Based Gate Driver IC for WBG Power Switches, in: IEEE Trans. Components, Pac, 2013: pp. 1768–1775.

[7] T. Fan, H. Zhang, P. Shang, C. Li, C. Chen, J. Wang, Z. Liu, H. Zhang, K. Suganuma, Effect of electroplated Au layer on bonding performance of Ag pastes, J. Alloys Compd. 731 (2018) 1280–1287.

[8] C. Buttay, D. Planson, B. Allard, D. Bergogne, P. Bevilacqua, C. Joubert, M. Lazar, C. Martin, H. Morel, D. Tournier, C. Raynaud, State of the art of high temperature power electronics, Mater. Sci. Eng. B Solid-State Mater. Adv. Technol. 176 (2011) 283–288.

[9] J. Dai, J. Li, P. Agyakwa, M. Corfield, C.M. Johnson, Comparative thermal and structural characterization of sintered nano-silver and high-lead solder die attachments during power cycling, IEEE Trans. Device Mater. Reliab. 18 (2018)

256–265.

[10] W. Loh, M. Corfield, H. Lu, S. Hogg, T. Tilford, C.M. Johnson, Wire bond reliability effect of bonding temperature, in: 2007 Int. Conf. Therm. Mech. Multi-Physics Simul. Exp. Microelectron. Micro-Systems., 2007.

[11] M.A. Eleffendi, L. Yang, P. Agyakwa, C. Mark Johnson, Quantification of cracked area in thermal path of high-power multi-chip modules using transient thermal impedance measurement, Microelectron. Reliab. 59 (2016) 73–83.

[12] W.D. Zhuang, P.C. Chang, F.Y. Chou, R.K. Shiue, Effect of solder creep on the reliability of large area die attachment, Microelectron. Reliab. 41 (2001) 2011–2021.

[13] A. Roshanghias, G. Bruckner, A. Binder, High temperature MEMS packages: die-attach solutions for LiNbO3 under low bonding pressures, J. Mater. Sci. Mater. Electron. 28 (2017) 8784–8792.

[14] L. Coppola, D. Huff, F. Wang, R. Burgos, D. Boroyevich, Survey on high-temperature packaging materials for SiC-based power electronics modules, in: PESC Rec. - IEEE Annu. Power Electron. Spec. Conf., 2007: pp. 2234–2240.

[15] T. McNutt, B. Passmore, J. Fraley, B. McPherson, R. Shaw, K. Olejniczak, A. Lostetter, High-Performance, Wide-Bandgap Power Electronics, J. Electron. Mater. 43 (2014) 4552–4559.

[16] R. Thokala, J. Chaudhuri, Calculated elastic constants of wide band gap semiconductor thin films with a hexagonal crystal structure for stress problems, Thin Solid Films. 266 (1995) 189–191. [17] H. Ma, J.C. Suhling, A review of mechanical properties of lead-free solders for electronic packaging, J. Mater. Sci. 44 (2009) 1141–1158.

[18] D.G. Ivey, Microstructural characterization of Au/Sn solder for packaging in optoelectronic applications, Micron. 29 (1998) 281–287.

[19] J.W. Yoon, H.S. Chun, S.B. Jung, Reliability evaluation of Au-20Sn flip chip solder bump fabricated by sequential electroplating method with Sn and Au, Mater. Sci. Eng. A. 473 (2008) 119–125.

[20] V. Chidambaram, H.B. Yeung, G. Shan, Reliability of Au-Ge and Au-Si eutectic solder alloys for high-temperature electronics, J. Electron. Mater. 41 (2012) 2107–2117.

[21] F. Lang, H. Yamaguchi, H. Ohashi, H. Sato, Improvement in joint reliability of SiC power devices by a diffusion barrier between Au-Ge solder and Cu/Ni(P)-metalized ceramic substrates, J. Electron. Mater. 40 (2011) 1563–1571.

[22] V. Chidambaram, J. Hattel, J. Hald, High-temperature lead-free solder alternatives, Microelectron. Eng. 88 (2011) 981–989.

[23] T. Nagaoka, Y. Morisada, M. Fukusumi, T. Takemoto, Selection of soldering temperature for ultrasonic-assisted soldering of 5056 aluminum alloy using Zn-Al system solders, J. Mater. Process. Technol. 211 (2011) 1534–1539.

[24] M. Rettenmayr, P. Lambracht, B. Kempf, C. Tschudin, Zn-Al based alloys as Pb-free solders for die attach, J. Electron. Mater. 31 (2002) 278–285.

[25] J.-E. Lee, K.-S. Kim, K. Suganuma, J. Takenaka, K. Hagio, Interfacial Properties of Zn–Sn Alloys as High Temperature Lead-Free Solder on Cu Substrate, Mater. Trans. 46 (2005) 2413–2418.

[26] J.M. Song, H.Y. Chuang, Z.M. Wu, Interfacial reactions between Bi-Ag high-temperature solders and metallic substrates, J. Electron. Mater. 35 (2006) 1041–1049.

[27] S.W. Chen, P.Y. Chen, C.H. Wang, Lowering of Sn-Sb alloy melting points caused by substrate dissolution, J. Electron. Mater. 35 (2006) 1982–1985.

[28] K. Suganuma, S.J. Kim, K.S. Kim, High-temperature lead-free solders: Properties and possibilities, Jom. 61 (2009) 64–71.

[29] G. Zeng, S. McDonald, K. Nogita, Development of high-temperature solders: Review, Microelectron. Reliab. 52 (2012) 1306–1322.

[30] C. Oh, S. Nagao, T. Kunimune, K. Suganuma, Pressureless wafer bonding by turning hillocks into abnormal grain growths in Ag films, Appl. Phys. Lett. 104 (2014) 3–7.

[31] C. Oh, S. Nagao, T. Sugahara, K. Suganuma, Pressureless Ag Thin-Film Die-Attach for SiC Devices, Mater. Sci. Forum. 821–823 (2015) 919–922.

[32] C. Oh, S. Nagao, K. Suganuma, Silver stress migration bonding driven by thermomechanical stress with various substrates, J. Mater. Sci. Mater. Electron. 26 (2015) 2525–2530.

[33] C. Oh, S. Nagao, T. Sugahara, K. Suganuma, Hillock growth dynamics for Ag stress migration bonding, Mater. Lett. 137 (2014) 170–173.

[34] S. Noh, C. Choe, C. Chen, K. Suganuma, Heat-resistant die-attach with cold-rolled Ag sheet, Appl. Phys. Express. 11 (2018).

[35] S. Lin, S. Nagao, E. Yokoi, C. Oh, H. Zhang, Y. Liu, K. Suganuma, Nano-volcanic Eruption of Silver, Sci. Rep. (2016) 34769.

[36] S.K. Sharma, S.U.M. Rao, N. Kumar, Hillock formation and agglomeration in silver films prepared by thermal evaporation, Thin Solid Films. 142 (1986) 95–98.

[37] S.K. Sharma, J. Spitz, Hillock formation, hole growth and agglomeration in thin

silver films, Thin Solid Films. 65 (1980) 339–350.

[38] C. Chen, S. Noh, H. Zhang, C. Choe, J. Jiu, S. Nagao, K. Suganuma, Bonding technology based on solid porous Ag for large area chips, Scr. Mater. 146 (2018) 123–127.

[39] H. Zhang, W. Li, Y. Gao, H. Zhang, J. Jiu, K. Suganuma, Enhancing Low-Temperature and Pressureless Sintering of Micron Silver Paste Based on an Ether-Type Solvent, J. Electron. Mater. 46 (2017) 5201–5208.

[40] H. Zhang, Y. Gao, J. Jiu, K. Suganuma, In situ bridging effect of Ag_2O on pressureless and low-temperature sintering of micron-scale silver paste, J. Alloys Compd. 696 (2017) 123–129.

[41] Y. Akada, H. Tatsumi, T. Yamaguchi, A. Hirose, T. Morita, E. Ide, Interfacial Bonding Mechanism Using Silver Metallo-Organic Nanoparticles to Bulk Metals and Observation of Sintering Behavior, Mater. Trans. 49 (2008) 1537–1545.

[42] T. Morita, Y. Yasuda, E. Ide, Y. Akada, A. Hirose, Bonding Technique Using Micro-Scaled Silver-Oxide Particles for <I>In-Situ</I> Formation of Silver Nanoparticles, Mater. Trans. 49 (2008) 2875–2880.

[43] S. Soichi, K. Suganuma, Low-temperature and low-pressure die bonding using thin Ag-flake and Ag-particle pastes for power devices, IEEE Trans. Components, Packag. Manuf. Technol. 3 (2013) 923–929.

[44] J. Jiu, H. Zhang, S. Koga, S. Nagao, Y. Izumi, K. Suganuma, Simultaneous synthesis of nano and micro-Ag particles and their application as a die-attachment material, J. Mater. Sci. Mater. Electron. 26 (2015) 7183–7191.

[45] S. Wang, H. Ji, M. Li, C. Wang, Fabrication of interconnects using pressureless low temperature sintered Ag nanoparticles, Mater. Lett. 85 (2012) 61–63.

[46] H. Alarifi, A. Hu, M. Yavuz, Y.N. Zhou, Silver nanoparticle paste for low-temperature bonding of copper, J. Electron. Mater. 40 (2011) 1394–1402.

[47] J. Yan, G. Zou, A. Wu, J. Ren, J. Yan, A. Hu, L. Liu, Y. Norman Zhou, Effect of PVP on the low temperature bonding process using polyol prepared Ag nanoparticle paste for electronic packaging application, J. Phys. Conf. Ser. 379 (2012).

[48] T. Morita, E. Ide, Y. Yasuda, A. Hirose, K. Kobayashi, Study of bonding technology using silver nanoparticles, Japanese J. Appl. Physics, Part 1 Regul. Pap. Short Notes Rev. Pap. 47 (2008) 6615–6622.

[49] Z.Z. Zhang, G.Q. Lu, Pressure-assisted low-temperature sintering of silver paste as an alternative die-attach solution to solder reflow, IEEE Trans. Electron. Packag. Manuf. 25 (2002) 279–283.

[50] Y. Morisada, T. Nagaoka, M. Fukusumi, Y. Kashiwagi, M. Yamamoto, M. Nakamoto, H. Kakiuchi, Y. Yoshida, A low-temperature pressureless bonding process using a trimodal mixture system of Ag nanoparticles, J. Electron. Mater. 40 (2011) 2398–2402.

[51] G. Zou, J. Yan, F. Mu, A. Wu, J. Ren, A. Hu, Low Temperature Bonding of Cu Metal through Sintering of Ag Nanoparticles for High Temperature Electronic Application, Open Surf. Sci. J. 3 (2014) 70–75.

[52] H. Nishikawa, X. Liu, X. Wang, A. Fujita, N. Kamada, M. Saito, Microscale Ag particle paste for sintered joints in high-power devices, Mater. Lett. 161 (2015) 231–233.

[53] S. Sakamoto, S. Nagao, K. Suganuma, Thermal fatigue of Ag flake sintering die-attachment for Si/SiC power devices, J. Mater. Sci. Mater. Electron. 24 (2013)

2593–2601.

[54] K. Suganuma, S. Sakamoto, N. Kagami, D. Wakuda, K.S. Kim, M. Nogi, Low-temperature low-pressure die attach with hybrid silver particle paste, Microelectron. Reliab. 52 (2012) 375–380.

[55] H. Zhang, S. Nagao, K. Suganuma, Addition of SiC Particles to Ag Die-Attach Paste to Improve High-Temperature Stability; Grain Growth Kinetics of Sintered Porous Ag, J. Electron. Mater. 44 (2015) 3896–3903.

This page is left blank intentionally.

Chapter 2

Fast and low-temperature sintering of micron/ submicron particles Ag paste by *in-situ* formation of nanoparticles

2.1 Introduction

Ag sintering technology is one of the most advantageous methods that can be used to realize high thermal and electrical conductivities of interconnections at a much lower temperature than the melting point of Ag. The advantageous properties enable this method to be applied as an interconnecting method for assembling wide band gap (WBG) semiconductor power electronics and also for flexible plastic electronics, which require highly reliable as well as low temperature fabrication capability [1,2]. Currently, Ag sinter die attach and wiring show great potential as novel highly conductive and heat-resistant bonding and wiring solutions for new power devices.

It was believed that sintering of conventional micron-sized silver particles requires a high sintering pressure of ~10–40 MPa and a high sintering temperature of ~300 °C [3–5]. As semiconductor chips and ceramic insulating substrates are brittle and vulnerable to harsh process conditions, and could suffer severe warpage or cracking during such a fabrication process, much effort has been focused on reducing sintering temperature and pressure. Therefore, nanoparticles (NPs) have been employed as interconnecting materials because they have high surface energy, which serves as a main driving force for the sintering process. Sintering of Ag NPs can be achieved even at room temperature without applying pressure [2,6,7]. However, a significant amount of an appropriate ligand (organic material) is required to protect the surface of Ag NPs to prevent their aggregation, because of their high surface energy. Such organic ligands used in the synthesis of NPs are known to inhibit the sintering of particles, and the die-attach procedure requires special treatments such as washing processes and high-temperature heating [8].

Furthermore, the extremely high cost of Ag NPs also hinders their applications. Therefore, Ag sinter joining and wiring with micron-sized Ag flakes, instead of NPs, have emerged as promising approaches for WBG power device packaging [1,9]. Robust interconnections can be successfully created using Ag flakes at a low temperature of 200 °C without any applied pressure, and the application of micron-sized Ag particles to power electronics has become a cornerstone [9].

Our group developed a hybrid Ag particle paste composed of micron-sized Ag flakes and submicron Ag particles for high-temperature applications [1]. The high packing density of the hybrid Ag paste can lead to electrical/thermal conductivity as well as bonding strength, while the paste costs much less compared to those based on NPs. Recently, bimodal Ag particles (micron and submicron sized particles) fabricated by a polyol process (denoted as polyol Ag particles) were applied for heat-resistant die attach, and they also performed well in Ag sinter joining [10]. The polyol Ag particles have lower surface energy than the hybrid Ag particles due to low specific surface ratio. Ag flakes have high specific surface area, which results in high surface energy [9]. Nevertheless, an Ag paste based on polyol Ag particles could successfully yield joints with high shear strength of more than 40 MPa and low resistivity at 200 °C, without any need for heating at higher temperature ~300 °C under high pressure 10–50 MPa [10]. The sintering behavior of the micron-sized polyol Ag particles is, however, not clear. It is speculated that other factors rather than the surface energy influence sintering process. Therefore, the sintering behavior of a paste composed of polyol Ag particles was investigated in this work. The results are compared with those of the Ag hybrid paste heated at low temperature 175 °C without any applied pressure.

2.2 Experimental methods

2.2.1 Preparation of Ag paste

Bimodal Ag particles were prepared by a polyol method as follows: in the first step, 0.5 g of polyvinylpyrrolidone (PVP, MW = 360,000) was dissolved in 50 g of ethylene glycol (EG) with magnetic stirring at room temperature. Then, 1.0 g of silver nitrate ($AgNO_3$) was added to the PVP solution and the mixture was heated at 150 °C for 1 h to allow the formation of Ag particles. During the first 30 min of the reaction, another mixture comprising 1.0 g of $AgNO_3$ and 50 g of EG was added dropwise. Finally, the precipitate formed was washed with acetone and ethanol to remove excess PVP and impurities.

The Ag powders obtained after drying the precipitate in air comprised of bimodal particles (Fig. 2.1a) with average diameters of ~0.4 and 3 μm. This powder was mixed with EG (8 wt.%) using a mixer for 5 min to obtain hybrid Ag particle paste. For convenience, the obtained Ag particles and the paste are referred to as “P paste filler” and “P paste,” respectively. Further, another Ag paste was prepared by the same method by mixing Ag flakes (AgC239, Fukuda Metal Foil and Powder Co., Ltd.) with an average diameter of 8 μm and Ag submicron particles (FHD, Mitsui Mining and Smelting Co., Ltd.) with an average diameter of 0.3 μm with EG (8 wt.%). This paste and the mixed Ag particles are referred as “A paste” and “A paste filler,” respectively. Fig. 2.1b shows the microstructure of the “A paste filler.” The preparation process is shown in Fig 2.2.

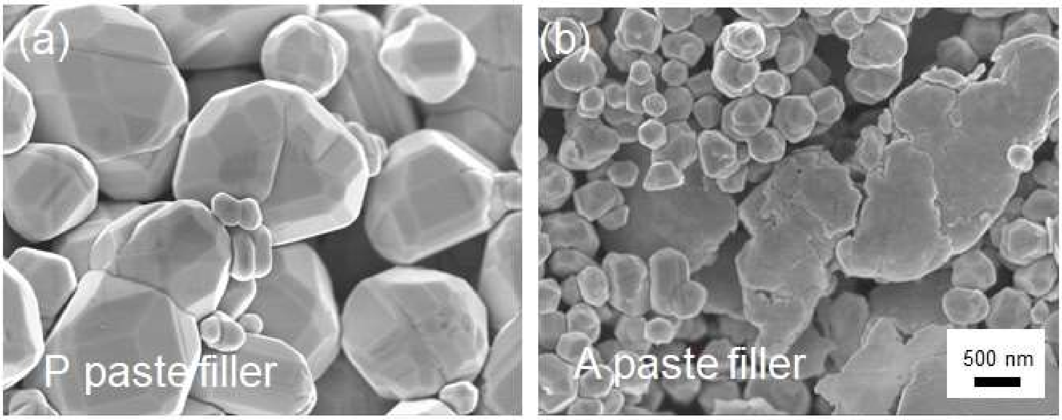

Fig. 2.1 Scanning electron microscope images of the two kinds of silver fillers: (a) P paste filler and (b) A paste filler

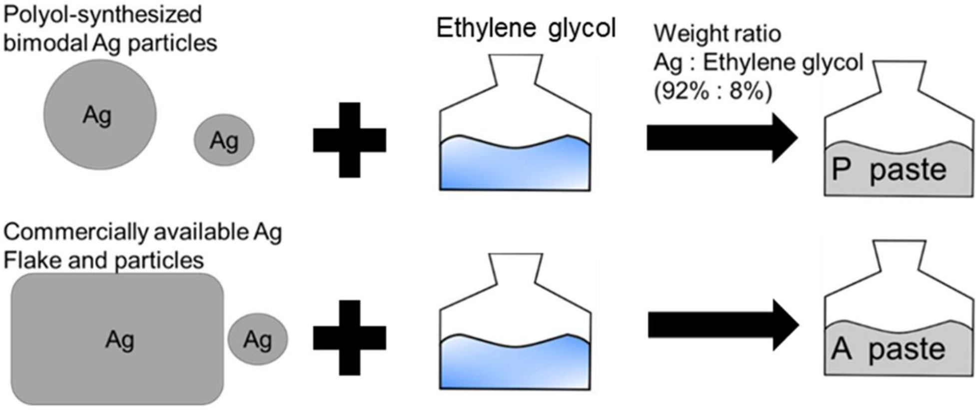

Fig. 2.2 Schematic diagram of Ag pastes preparation process

2.2.2 Characterization of the Ag paste and Ag particles

The specific surface area of the Ag particles was determined by a nitrogen gas sorption analysis (Nova 4200e, Quantachrome), and the average size of the Ag particles are listed in Table 2.1. A paste filler has higher specific area than P paste filler, which corresponds to a higher surface energy. The cross-sectional samples for electron microscopy were prepared using a focused ion beam (FIB, FIB-2100, HITACHI). Cross-sectional scanning electron microscopy (SEM, SU-8020, Hitachi) and scanning ion microscope (SIM, FIB-

2100, HITACHI) images were obtained at a tilting angle of 30°. The grain size of A paste filler and P paste filler was determined by SEM (see Fig. 2.2). Transmission electron microscopy (TEM) images were obtained using JEM-ARM200F, JEM-2100 (JEOL).

Table 2.1 Properties of the two types of Ag fillers

Type of Ag filler	Shape	Average size	Specific surface area
Ag flakes and Submicron Ag particles “A paste filler”	Flake, Spherical	8 µm (0.26 µm thickness), 0.3 µm	1.33 m^2/g, 1.56 m^2/g
Polyol synthesized Ag particles “P paste filler”	Spherical	0.4 µm (small) 2.5 µm (large)	0.62 m^2/g

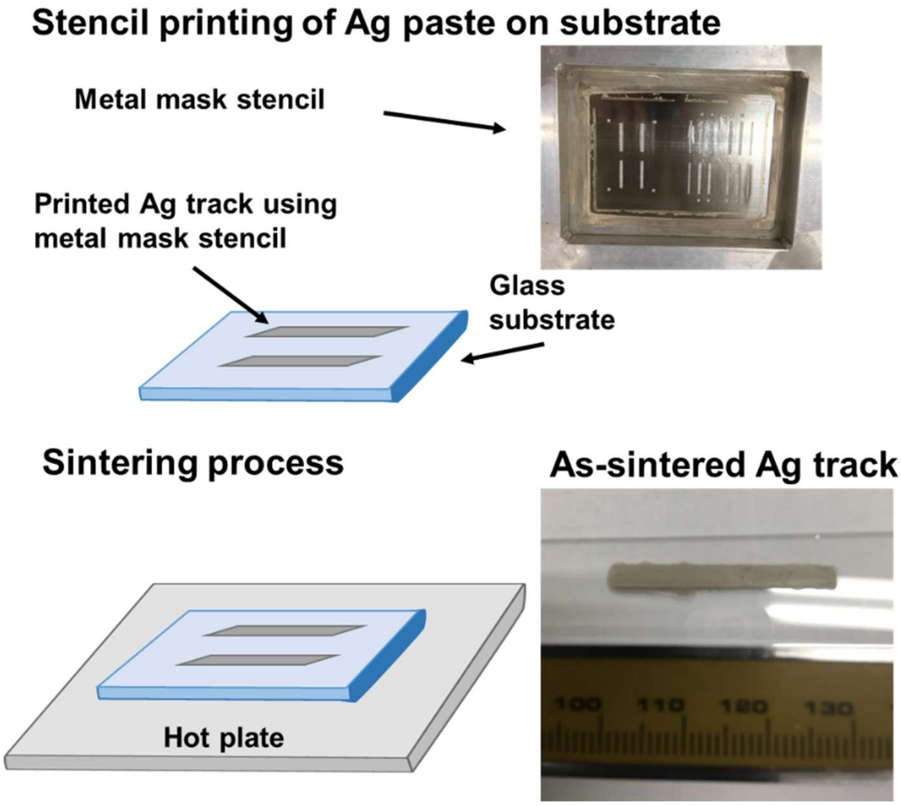

Fig. 2.3 Schematic diagram of sample preparation process

Sintering behavior of the Ag pastes was evaluated by measuring electric resistivity of the printed tracks on a glass substrate after sintering. The Ag tracks were first heated at 150 °C for 5 min to evaporate the organic molecules under mild conditions, and then heated at 175 °C on a hot plate in air to allow particle sintering. The process is illustrated in Fig. 2.3. X-ray photoelectron spectroscopy (XPS, JPS-9010MX, JEOL) was conducted to analyze the surface chemical states of Ag particles using Al-Kα radiation (1486.6 eV), and the spectra were calibrated with the C1s peak at 284.8 eV as the internal standard. To analyze the composition of Ag particles in more detail, 1.0 g of Ag particles was suspended in 100 ml of ethanol and the suspension was filtered using a centrifugal ultrafilter (Amicon Ultra-153K, Millipore, MA) with porous cellulose membranes with a nominal particle size limit of 1–2 nm through centrifugation for 30 min at 3500 rpm. Then, the supernatants were analyzed by inductively coupled plasma atomic emission spectroscopy (ICP-AES, ICPS-8100, Shimadzu) and UV-vis spectroscopy (V-770, JASCO). The thermal behaviors of Ag fillers and pastes were evaluated by thermogravimetric analysis (TGA) and differential thermal analysis (DTA) (2000SE, NETZSCH) at a heating rate of 10 °C·min^{-1}.

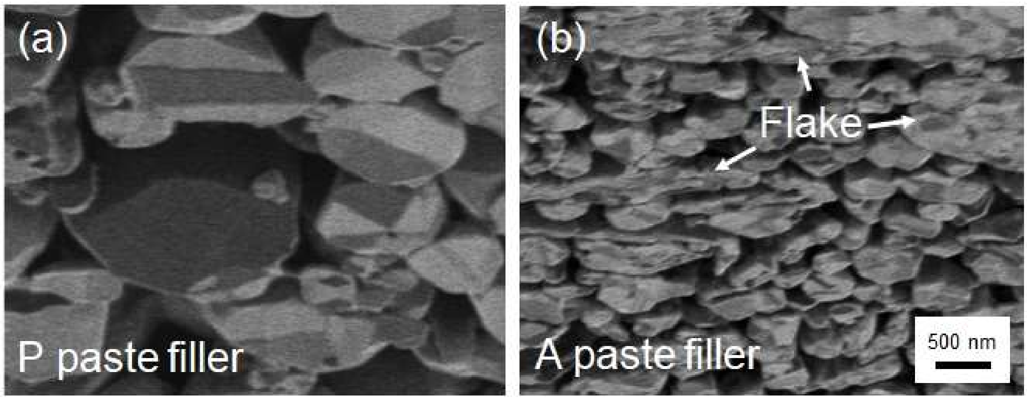

Fig. 2.4 Cross-sectional scanning ion microscope images of (a) P paste filler and (b) A paste filler

2.3 Results and discussion

2.3.1 Electrical resistivity of sintered Ag wiring

Since electrical resistivity is known to be a sensitive parameter for evaluating the sintering or densifying of sintered metallic materials, the electrical resistivity of Ag tracks was measured after sintering them at 175 °C. Fig. 2.5a shows the electrical resistivity of Ag tracks derived from the two pastes as a function of sintering time. The electrical resistivity of the sintered tracks of A paste decreased to the order of 10^{-4} Ω·cm after 5 min, and with further heating, it decreased slowly to ~1.30×10^{-5} Ω·cm after 1 h. Surprisingly, the resistivity of the sintered tracks of P paste decreased to a much lower value of 9.8×10^{-6} Ω·cm after only 5 min, indicating the rapid sintering ability of P paste, and the resistivity decreased further with further heating, as shown in Fig. 2.5a. The difference in sintering speed is not obvious because A paste filler has a smaller grain size and higher specific surface area, (Fig. 2.4 and Table 2.1), and these parameters are known to accelerate sintering. Regardless of the fast sintering ability of P paste, the change tendency of electrical resistivity is consistent with the cross-sectional microstructures of sintered Ag tracks shown in Fig. 2.5b and Fig. 2.5c. P paste sintered well and necking had formed well even after a short sintering time of 5 min, as shown in Fig. 2.5b. Furthermore, Ag NPs formed around the necking locations of the Ag tracks of P paste, as indicated in Fig. 2.5b. These self-produced particles are identified as Ag NPs by TEM characterization, as shown in Fig. 2.5d. In contrast, no apparent necking can be observed in the Ag tracks of A paste after sintering, as shown in Fig. 2.5c. It is well known that Ag NPs have high surface energy, and low melting temperature, which are expected to accelerate the sintering of P paste at a low temperature. However, A paste did not show the formation of

Ag NPs at 175 °C, as shown in Fig. 2.5c. To understand the fast sintering of P paste, further analysis was conducted to clarify the formation mechanism of Ag NPs.

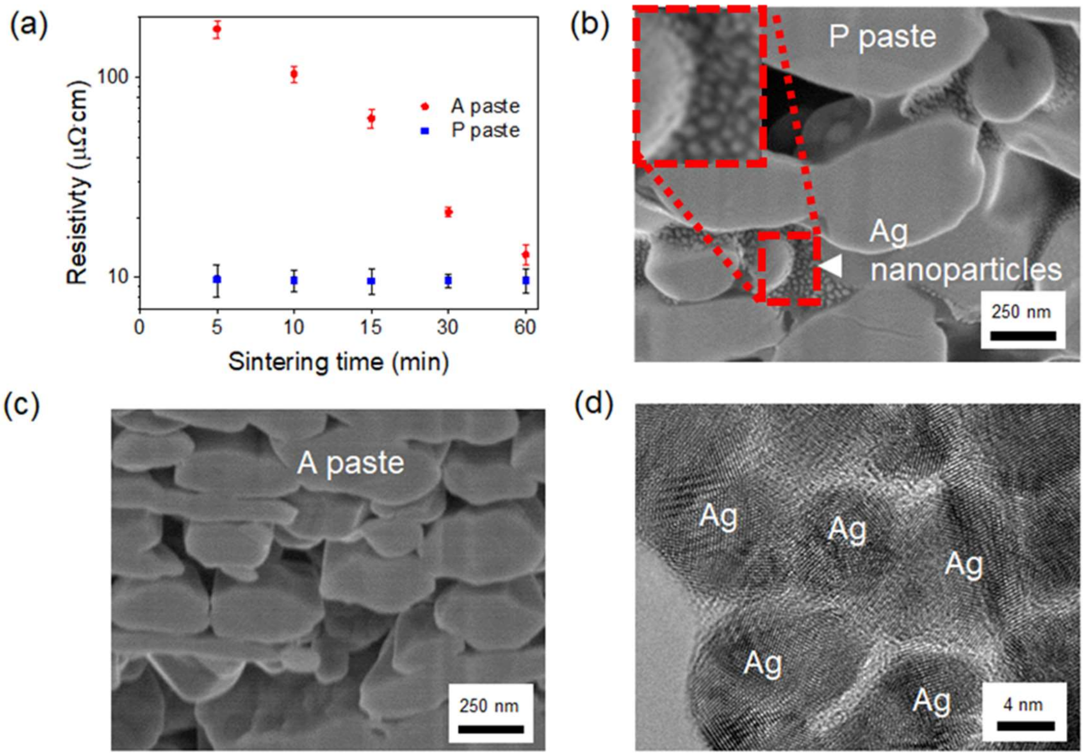

Fig. 2.5 Changes in the electrical resistivity of Ag tracks and their microstructures after sintering at 175 °C. (a) Change in the electrical resistivity of Ag tracks with sintering time. Cross-sectional scanning electron microscopy images of the wirings from (b) P paste and (c) A paste after sintering for 5 min. The images were obtained at a tilting angle of 30°. Inset figure of (b) represents enlarged image of *in situ* formed Ag nanoparticles. (d) HR-TEM image of the sintered Ag track derived from P paste. Mechanism of the formation of Ag NPs

It is well known that the reduction of Ag oxide with organic reducing agents can lead to the formation of Ag NPs at low temperatures below 175 °C [5,11]. Here, the surface states of P paste and A paste fillers were analyzed. The binding energy of O(1s) level is shown in the XPS spectra in Fig. 2.6a and 2.6b. The peaks with the binding energies of 530.0 and 530.3 eV correspond to adsorbed oxygen on Ag, and the other peaks at 531.3 and 533.8 eV are attributed to the oxygen in the C=O bond and C–O bonds of aryl ethers or esters and carboxylic acids, respectively [12–15]. Apparently, the binding energies of O(1s) of these two Ag fillers indicate the absence of bulk Ag oxide, because the peaks corresponding to Ag oxide at 528.5 and 529.2 eV did not appear [16,17]. Since Ag oxide is not detected on these two particles, it can be concluded that the observed Ag NPs do not originate from the reduction of the initially formed Ag oxides by in the presence of any organic residues. Further, it is known that Ag NPs formation can be attributed to the reduction of Ag ions [18,19]. Therefore, it was verified the presence of Ag ions using the following method: the supernatants of the ultra-filtered solutions recovered from Ag fillers mixed with ethanol were analyzed by ICP-AES.

The atomic emission spectra of supernatants are presented in Fig. 2.6c. The Ag concentration in the supernatant from P paste filler was determined to be 24.4 ppm, while that in the supernatant from A paste filler was found to be significantly lower at 0.4 ppm. This large difference between the Ag concentrations of the supernatants from the two fillers is expected to influence the formation of Ag NPs. During the fabrication of Ag particles by the polyol method, PVP is used as protective ligand for the uniform growth of Ag particles. Although Ag particles were washed to remove PVP, some residual PVP remains on the surface of Ag particles, as verified by UV-vis spectroscopy.

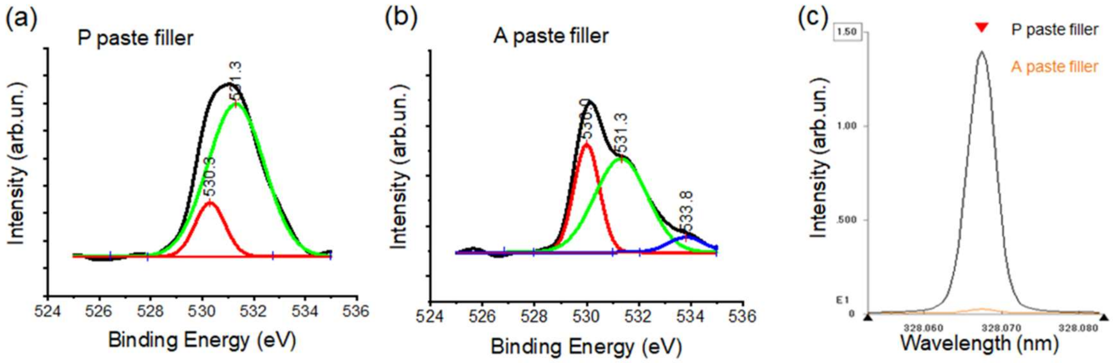

Fig. 2.6 XPS O (1s) spectra of (a) P paste filler and (b) A paste filler. The colored lines represent the deconvoluted spectra. (c) ICP–AES results of the supernatant of Ag fillers mixed with ethanol filtered through an Amicon centrifugal ultrafilter (Amicon Ultra- 15 3K, Millipore, MA).

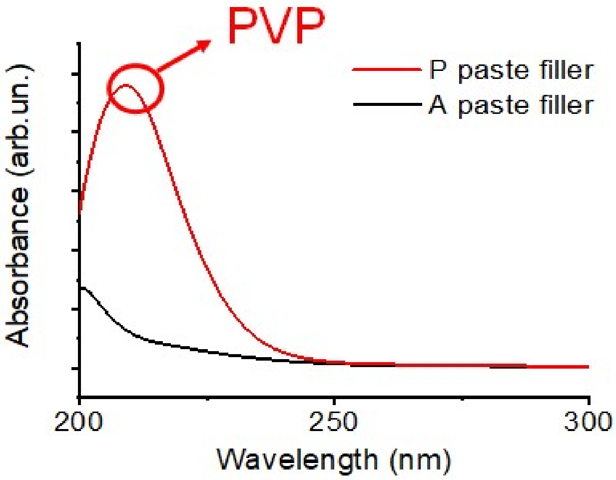

Fig. 2.7 UV-vis spectra of the supernatants of Ag fillers mixed with ethanol filtered through an Amicon centrifugal ultrafilter (Amicon Ultra- 15 3K, Millipore, MA).

The UV-vis spectrum of the particles has an absorption band near 213 nm (Fig. 2.7) [20]. PVP (MW = 360,000) decomposes at ~400–450 °C [21]. Thus, its presence is not the main reason for the fast sintering of the Ag paste. PVP is known to cap Ag ions or produce a complex with Ag ions [21–23]. The interaction between Ag^+ and PVP to form a coordinative complex with the involvement of electrons from oxygen or nitrogen atoms of PVP (1) and the reduction of Ag^+ (2) can occur, as shown in Eq. 1 and 2 [22–24]:

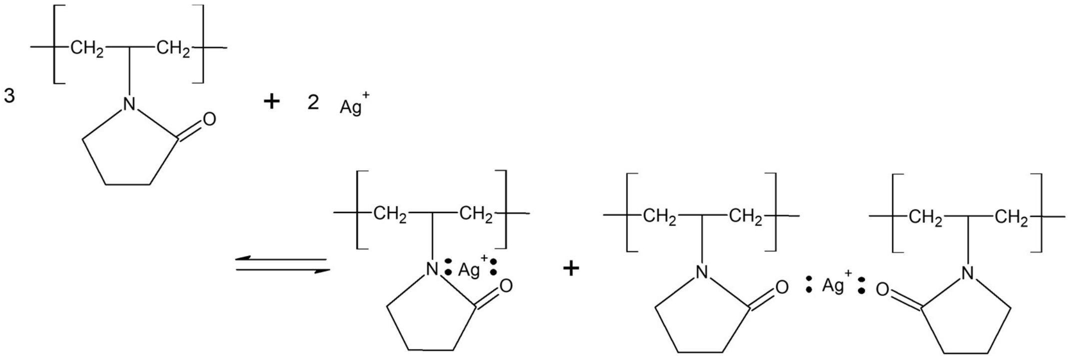

(1)

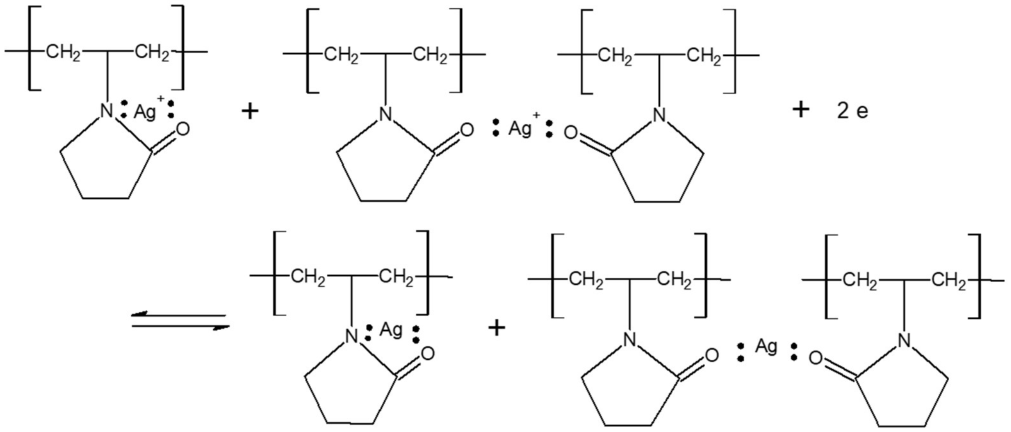

(2)

EG is generally used as a reductant to produce Ag particles. Therefore, Ag NPs are expected to be generated by the reduction of Ag ions or Ag-PVP complex by EG during the sintering process [18,19].

It was tried to sinter the two Ag fillers in the absence of EG and only P paste filler failed to sinter and a powder-like material formed even when it was heated up to 250 °C. Therefore, the reduction of Ag+ ions is expected to be the main mechanism responsible for the fast sintering of P paste. Ag NPs produced by the reaction can serve as a nanobinder to accelerate sintering process. This phenomenon might explain the observed electrical resistivity and the previously reported high shear strength >40 MPa under the mild sintering condition of 200 °C and 0.4 MPa pressure for P paste filler [10].

To further investigate the sintering mechanism of the Ag pastes, the thermodynamic properties of the two Ag fillers and Ag pastes were evaluated by TGA-DTA. Regardless of the type of Ag particles or pastes, an exothermic peak with a slight mass decrease at ~250 °C was observed, as shown in Figs. 2.8a–d. This result indicates that the peak originates from these Ag particles. The exothermic reaction of Ag particles with a slight mass decrease is attributed to the decomposition of organic residues adsorbed on their surface [25]. However, a new exothermic peak was observed at ~180 °C in the curve for P paste, which did not appear in the TGA-DTA curve of P paste filler (Figs. 2.8a, c). Since P paste filler without EG does not have the exothermic peak shown in Fig. 2.8a for P paste, the peak can be attributed to the reaction between EG and P paste filler, which is expected to be the main mechanism for the fast sintering. To further evaluate the peak, TGA–DTA curve of A paste with added $AgNO_3$ was analyzed. A peak at ~180 °C was observed for this mixture, as shown in Fig. 2.8d, indicating that the peak near 180 °C represents the reduction of Ag^+ ions.

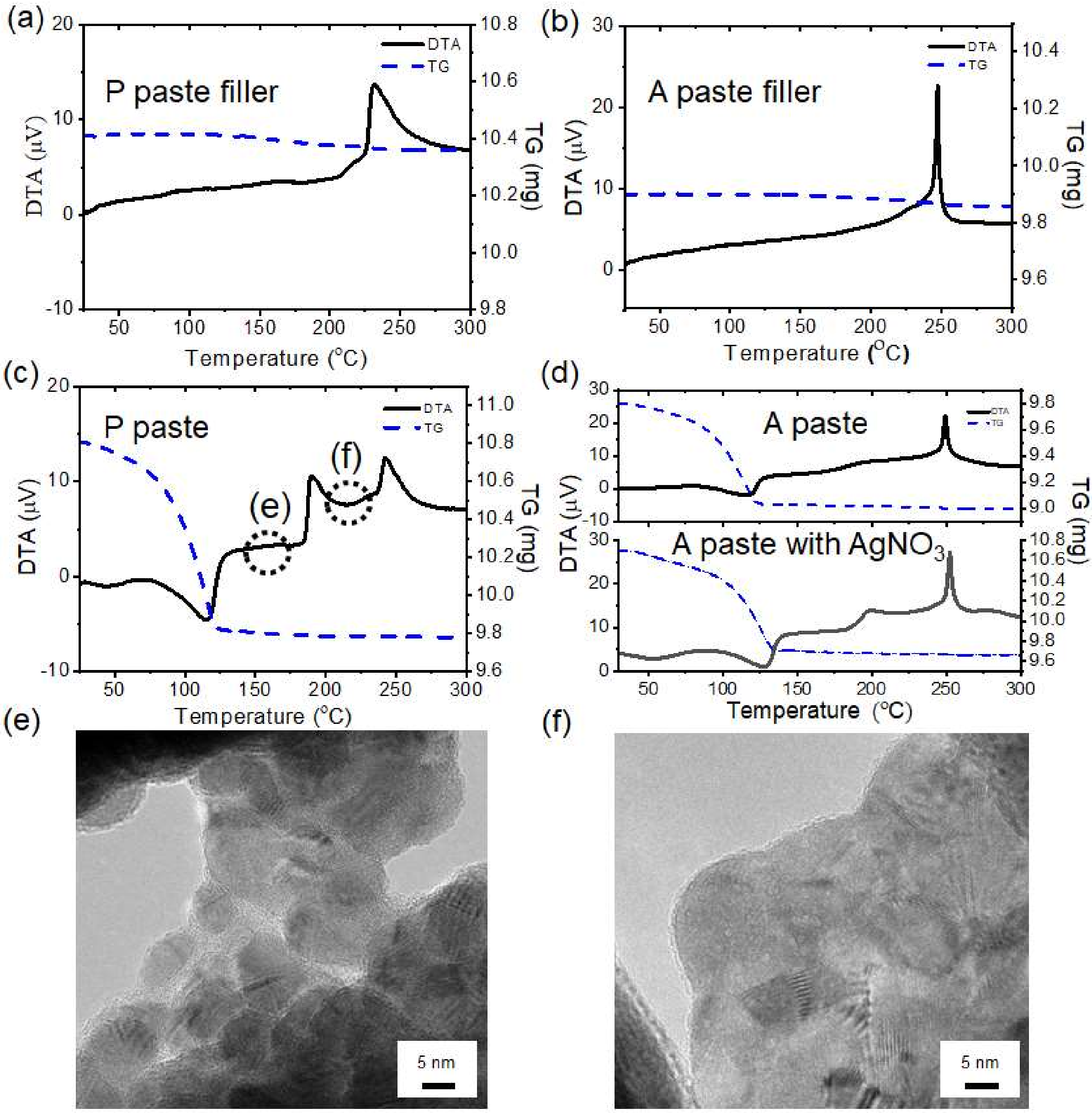

Fig. 2.8 TGA–DTA data of (a) P paste filler, (b) A paste filler, (c) P paste, and (d) A paste, and A paste with added $AgNO_3$. Microstructures of sintered Ag tracks derived from P paste sintered at (e) 150 °C and (f) 200 °C for 1 min.

The microstructure of P paste was observed by TEM before and after the observation of the peak at ~180 °C in the DTA curve, and the images are shown in Figs. 2.8e–f. Self-produced Ag NPs can be observed below the peak temperature, as shown in Fig. 2.8e, and a well-densified structure of the Ag wiring is observed after the peak, as shown in Fig. 2.8f. When the pastes are heated above 150 °C, the organic residues will be removed and the sintering of Ag particles starts [6]. Layers of organic materials are still adsorbed on the Ag particles during the sintering process below 150 °C, and the organic materials can prevent the sintering of Ag particles. Therefore, the peak at 180 °C can be attributed to the sintering of the self-produced NPs. Moon et al. [26] also indicated that the exothermic reaction in Ag NPs is due to the diffusion of unstable atoms on Ag NPs surface during the surface sintering reaction, which occurs at a lower temperature than in bulk materials.

Thus, the reason for the fast sintering of P paste can be summarized as follows: after P paste fillers are synthesized, there is residual PVP, which holds Ag ions or Ag-PVP complex on Ag particle surface. During the sintering process, Ag-PVP complex or Ag ions is reduced to Ag nanoparticles or contribute to Ag nucleation and growth, which can accelerate the necking of Ag particles, resulting in low resistivity of the wirings in a short time even sintered at a low temperature.

2.3.2 Verification of the sintering mechanism

To further prove the effect of Ag reduction on the low temperature sintering process, P paste filler was washed thoroughly with acetone and ethanol to obtain “washed P paste,” and the weight ratio of Ag to EG was kept the same as that of P paste. Approximately 1 wt.% of $AgNO_3$ was added to A paste to prepare “modified A paste.” The electrical resistivity of sintered Ag tracks obtained from the two new pastes is shown in Fig. 2.9. The electrical resistivity of the washed P paste decreased to ~3.96×10^{-5} Ω·cm after sintering for 5 min, and the resistivity is almost 4 times higher than that of the original P paste. The TEM analysis of the particles after the washing process also suggests the detachment of PVP after the supplementary washing process, due to the removal of Ag-PVP complex and Ag ions (See Fig. 2.10). After sintering for 30 min, no further decrease in the electrical resistivity of the wiring of washed P paste was observed with further heating, indicating that sintering of P paste cannot be achieved without the aid of high pressure and high temperature due to the presence of only submicron- and micron-sized particles without a significant amount of NPs. On the other hand, A paste with 1% of added $AgNO_3$ sintered rapidly, and the electrical resistivity of the wiring reached 4.03×10^{-5} Ω·cm after sintering for only 5 min at 175 °C, as shown in Fig. 2.9b. In contrast, the resistivity of the wiring of A paste was only 1.74×10^{-4} Ω·cm under the same sintering conditions. This result suggests in situ Ag ion reduction can improve the sintering ability of Ag particles. The fast sintering mechanism of P paste is shown in Fig. 2.11.

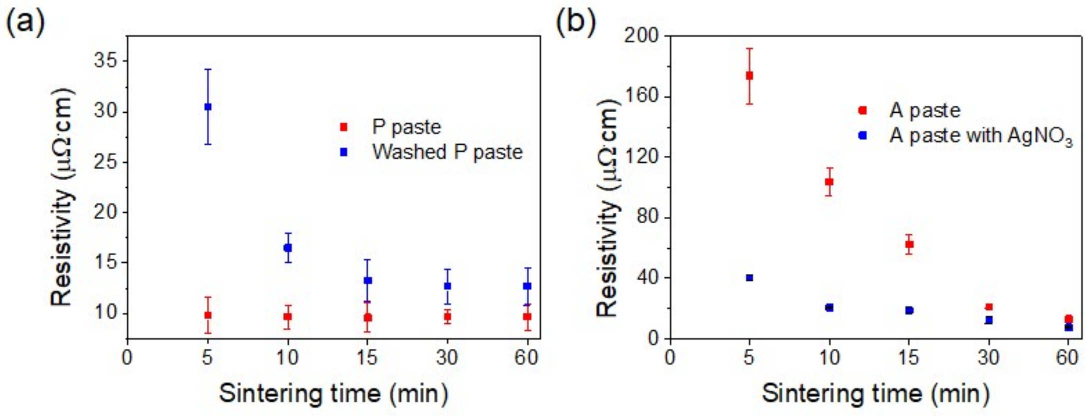

Fig. 2.9 Changes in the electrical resistivity of Ag tracks derived from two modified pastes after sintering at 175 °C: (a) Washed P paste and (b) A paste with added Ag ions

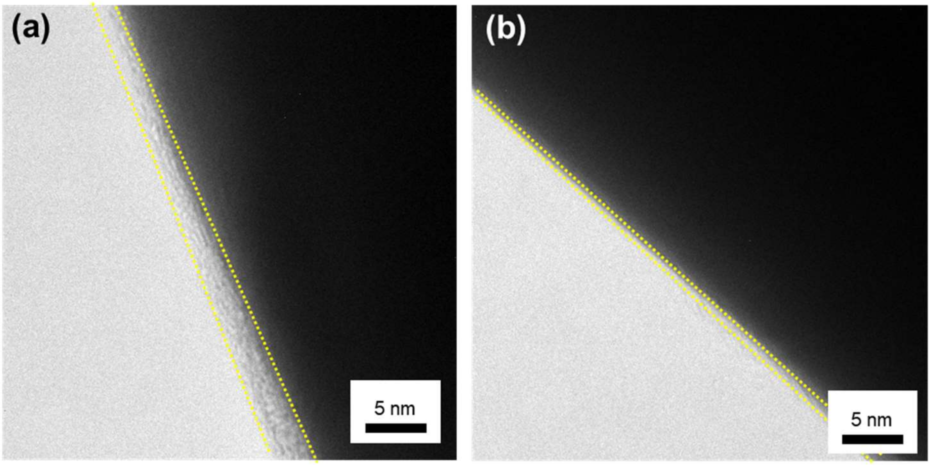

Fig. 2.10 TEM image showing the thickness of the PVP film on P paste fillers: before supplementary washing (a) and after supplementary washing (b)

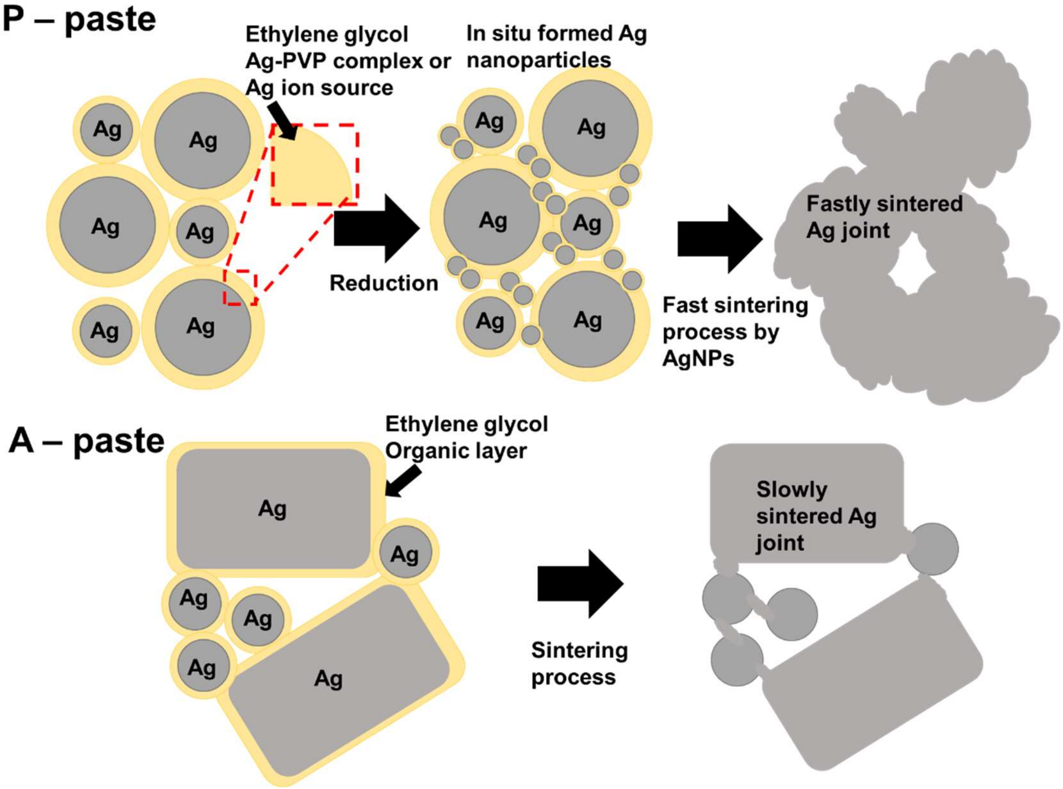

Fig. 2.11 Schematic diagram of sintering mechanism of Ag pastes.

2.4 Conclusion

The sintering mechanism of P paste was investigated. During the sintering process, in situ formed Ag NPs were observed only in Ag tracks derived from P paste sintered at 175 °C, and they are considered to be the main driving force for Ag particle sintering. Ag NPs are produced by the reduction of residual Ag ions by EG, which can reduce metal ions to atoms. The electrical resistivity of Ag wiring increased after residual Ag ions were washed away from the P particles. This result provides strong evidence for the hypothesis that the residual Ag ions can enhance sintering of Ag paste. Experimental evidences for proposed fast sintering mechanism by reduction reaction is summarized in Table 2.2. The method described herein provides a new way to lower sintering temperature and accelerate sintering process without any need for using expensive Ag NPs, and can be potentially applied to Ag sintering technology.

Table 2.2 Summary of evidences for fast sintering mechanism by reduction reaction.

	P- paste	A-paste
Ag ion concentration (the supernatants of Ag fillers mixed with ethanol filtered through an Amicon centrifugal ultrafilter)	High	Low
Particle sintering without solvent heating up to 250 °C	Almost not achieved (no exothermal reaction)	Well-achieved
paste sintering heating up to 175°C	Well-achieved (exothermal reaction is confirmed)	Slowly achieved
Sintering after washing process	decreased sintering speed	N/A
Sintering after $AgNO_3$ addition	N/A	increased sintering speed

References

[1] K. Suganuma, S. Sakamoto, N. Kagami, D. Wakuda, K.S. Kim, M. Nogi, Low-temperature low-pressure die attach with hybrid silver particle paste, Microelectron. Reliab. 52 (2012) 375–380.

[2] S. Magdassi, M. Grouchko, O. Berezin, A. Kamyshny, Triggering the sintering of silver nanoparticles at room temperature, ACS Nano. 4 (2010) 1943–1948.

[3] H. Schwarzbauer, R. Kuhnert, Novel Large Area Joining Technique for Improved Power Device Performance, in: IEEE Trans. Ind. Appl., 1991: pp. 93–95.

[4] K.S. Siow, Mechanical properties of nano-silver joints as die attach materials, J. Alloys Compd. 514 (2012) 6–19.

[5] H. Zhang, Y. Gao, J. Jiu, K. Suganuma, In situ bridging effect of Ag 2 O on pressureless and low-temperature sintering of micron-scale silver paste, J. Alloys Compd. 696 (2017) 123–129.

[6] D. Wakuda, K.S. Kim, K. Suganuma, Room temperature sintering of Ag nanoparticles by drying solvent, Scr. Mater. 59 (2008) 649–652.

[7] D. Wakuda, K.S. Kim, K. Suganuma, Ag nanoparticle paste synthesis for room temperature bonding, IEEE Trans. Components Packag. Technol. 33 (2010) 437–442.

[8] M.A. Asoro, D. Kovar, P.J. Ferreira, Effect of surface carbon coating on sintering

of silver nanoparticles: in situ TEM observations, Chem. Commun. 50 (2014) 4835–4838.

[9] S. Soichi, K. Suganuma, Low-temperature and low-pressure die bonding using thin Ag-flake and Ag-particle pastes for power devices, IEEE Trans. Components, Packag. Manuf. Technol. 3 (2013) 923–929.

[10] J. Jiu, H. Zhang, S. Koga, S. Nagao, Y. Izumi, K. Suganuma, Simultaneous synthesis of nano and micro-Ag particles and their application as a die-attachment material, J. Mater. Sci. Mater. Electron. 26 (2015) 7183–7191.

[11] Y. Suzuki, T. Ogura, M. Takahashi, A. Hirose, Low-current resistance spot welding of pure copper using silver oxide paste, Mater. Charact. 98 (2014) 186–192.

[12] A.I. Boronin, V.I. Bukhityarov, A.L. Vishnevskii, G.K. Boreskov, V.I. Savchenko, XPS and UPS studies of oxygen adsorption over clean and carbon-modified silver surfaces, Surf. Sci. 201 (1988) 195–210.

[13] V.I. Bukhtiyarov, V. V Kaichev, I.P. Prosvirin, Oxygen adsorption on Ag(111): X-ray photoelectron spectroscopy (XPS), angular dependent x-ray photoelectron spectroscopy (ADXPS) and temperature-programmed desorption (TPD) studies, J. Chem. Phys. 111 (2005) 2169–2175.

[14] Q. Xu, P. Pu, J. Zhao, C. Dong, C. Gao, Y. Chen, Preparation of highly photoluminescent sulfur-doped carbon dots for Fe (III) detection, J. Mater. Chem. A. 3 (2015) 542–546.

[15] L. Fan, S. Qiao, W. Song, M. Wu, X. He, X. Qu, Electrochimica Acta Effects of the functional groups on the electrochemical properties of ordered porous carbon for supercapacitors, Electrochim. Acta. 105 (2013) 299–304.

[16] T. Zhao, R. Sun, S. Yu, Z. Zhang, L. Zhou, H. Huang, R. Du, Size-controlled preparation of silver nanoparticles by a modified polyol method, Colloids Surfaces A Physicochem. Eng. Asp. 366 (2010) 197–202.

[17] J.F. Weaver, G.B. Hoflund, Surface Characterization Study of the Thermal Decomposition of Ag2O, Chem. Mater. 6 (1994) 1693–1699.

[18] R.D. Glover, J.M. Miller, J.E. Hutchison, Generation of metal nanoparticles from silver and copper objects: Nanoparticle dynamics on surfaces and potential sources of nanoparticles in the environment, ACS Nano. 5 (2011) 8950–8957.

[19] N. Matsuhisa, D. Inoue, P. Zalar, H. Jin, Y. Matsuba, A. Itoh, T. Yokota, D. Hashizume, T. Someya, Printable elastic conductors by in situ formation of silver nanoparticles from silver flakes, Nat. Mater. 16 (2017) 834–840.

[20] P. Tavlarakis, J. Urban, N. Snow, Determination of Total Polyvinylpyrrolidone

(PVP) in Ophthalmic Solutions by Size Exclusion Chromatography with Ultraviolet-visible Detection, J. Chromatogr. Sci. 49 (2014) 457–462.

[21] J. Jiu, K. Murai, K. Kim, K. Suganuma, Synthesis of silver nanorods and application for die attach material in devices, J. Mater. Sci. Mater. Electron. 21 (2010) 713–718.

[22] Z. Zhang, B. Zhao, L. Hu, PVP Protective Mechanism of Ultrafine Silver Powder Synthesized, J. Solid State Chem. 110 (1996) 105–110.

[23] J.J. Zhu, C.X. Kan, J.G. Wan, M. Han, G.H. Wang, High-yield synthesis of uniform Ag nanowires with high aspect ratios by introducing the long-chain PVP in an improved polyol process, J. Nanomater. 2011 (2011) 982547.

[24] C. Kan, C. Wang, J. Zhu, H. Li, Formation of gold and silver nanostructures within polyvinylpyrollidone (PVP) gel, J. Solid State Chem. 183 (2010) 858–865.

[25] S. Sakamoto, S. Nagao, K. Suganuma, Thermal fatigue of Ag flake sintering die-attachment for Si/SiC power devices, J. Mater. Sci. Mater. Electron. 24 (2013) 2593–2601.

[26] K. Moon, H.A.I. Dong, R. Maric, S. Pothukuchi, A. Hunt, Y.I. Li, Thermal Behavior of Silver Nanoparticles for Low-Temperature Interconnect

Applications, J. Electron. Mater. 34 (2005) 168–175.

This page is left blank intentionally.

Chapter 3

Ag particles for sinter joining: flakes or spheres?

3.1 Introduction

Ag sintering die-attach has emerged for WBG packaging. As Ag possesses the highest thermal and electrical conductivity in all metal elements, this advantage, along with its sufficiently high melting point, lead to sound bonding and enhanced operating performance. Interestingly, Ag NPs of less than 10-20 nm are capable of spontaneous sintering at low temperatures and even at room temperature with washing process. This spontaneous sintering is driven by an activated surface due to the extremely large surface/volume ratio [1,2]. However, application of a die-attach with Ag NPs typically requires high pressure and heating during sintering process to achieve stable bonding. This is mainly due to the organic dispersant or protection layer on particle surface formed for avoiding spontaneous agglomeration during both paste production and storage [3]. Such organic additives for nanoparticles tend to inhibit the sintering [3], and hence require special treatments like high pressure and heating during die-attach. The inevitable processes associated with the use of Ag NPs hinder the advantages of their low-temperature sintering and their acceptance as mass-produced die attaches in industry.

Micro or submicron sized Ag particles, therefore, appear more attractive than nanoparticles as they possess little organic additives and have a lower surface/volume ratio than nanoparticles. Hybridized submicron particles with Ag micro-flakes successfully applied to die-attach sinter joining for WBG devices demonstrated sufficiently high shear strength and electrical/thermal conductivity with acceptably mild conditions of the bonding process [4]. These Ag fillers have high levels of free energy due to their large specific surface, which is the main factor for sintering ability. However, without having deeper understanding of the process, sintering with Ag flakes and with spherical particles has been used empirically. In this chapter, sintering process was examined for both cases with Ag flake and with Ag spherical particles. Then, the merits of flake-shaped particles are clarified.

3.2 Experimental methods

3.2.1 Preparation of the Ag paste

Two types of Ag particles were selected from the well-established Ag pastes [4]. The first one consists of submicron spherical particles (Mitsui Mining and Smelting Co., Ltd., Japan) with an average diameter of 300 nm, and the second consists of flake particles (Fukuda Metal Foil and Powder Co., Ltd.) with an average diameter and thickness of 8 μm and 260 nm, respectively. In preparation of a Ag bonding paste, they were separately mixed with ethylene glycol (EG) at a weight ratio of 10:1 using a planetary mixer (HM-500, Keyence, Japan) for 5 min. Hereafter, the Ag pastes made of spherical particles and flake particles are referred to “S” and “F” paste, respectively.

3.2.2 Sintering process and evaluation of microstructure and shear strength

To evaluate the die-attach properties of the S and F pastes, Si dummy chips with dimensions of 3 mm ×3 mm × 0.5 mm and a Cu substrate with 140 mm × 90 mm × 0.8 mm have been prepared and both surfaces for bonding were metalized with Ti 100 nm / Ag 2000 nm layers by a sputtering process. Sample preparation process is illustrated in Fig. 3.1. Each chip was then sinter-joined to a Cu substrate with S or F paste at 250 °C for 60 min under a slightly applied pressure of 0.4 MPa in air. Shear strength of the obtained die-attach structure was measured by XD-7500 die-shear tester (Nordson-Dage, UK). One data point was obtained from eight samples of each paste tested for statistical averaging. The microstructures were observed by a scanning electron microscopy (SU8020, Hitachi, Japan) at an acceleration voltage, 5 kV, and a transmission electron microscopy (JEM-2100, JEOL, Japan) at an accelerating voltage 200 kV.

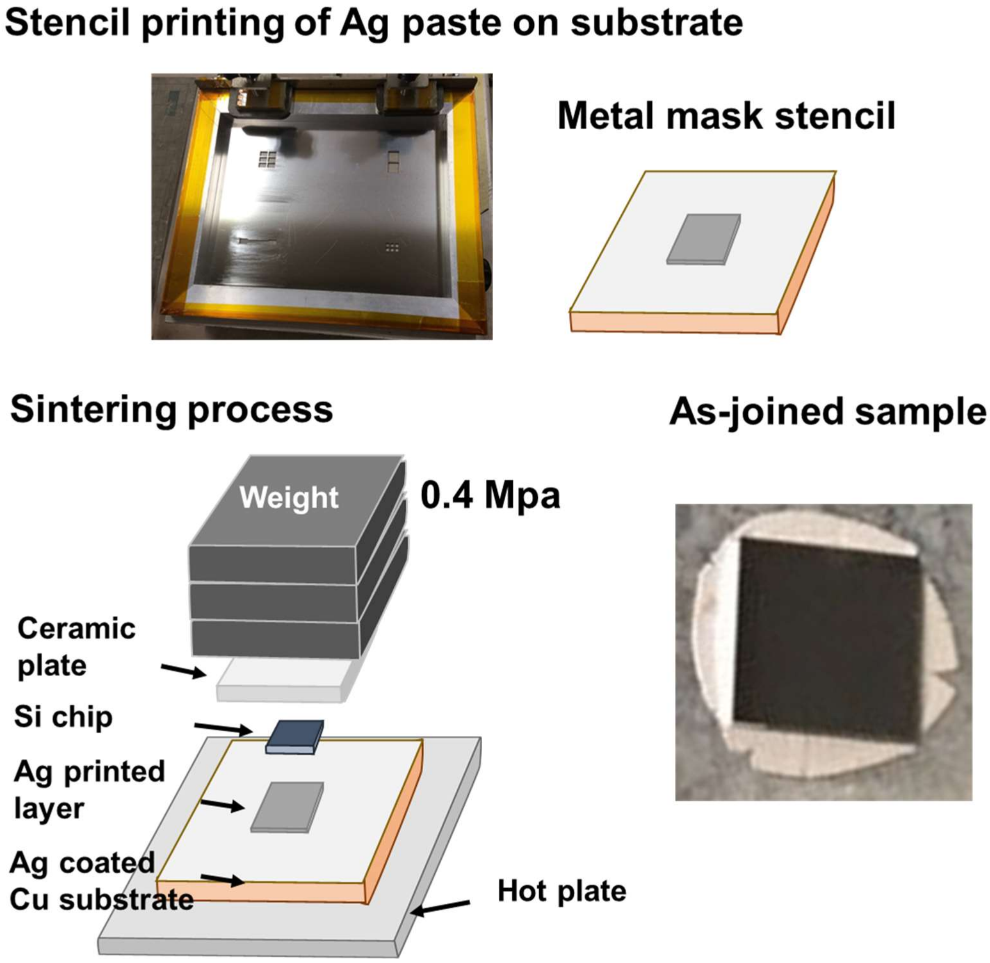

Fig. 3.1 Schematic diagram of sample preparation process

3.2.3 Residual microstrain analysis with X-ray diffraction

Residual microstrain and crystallite sizes in Ag particles and in sintered joint layer were measured by a line broadening analysis of powder X-ray diffractions (XRD) using a Smartlab diffractometer (Rigaku Corp., Japan) with Cu target. To minimize the effect of Cu Kα_2, a Ge (220) monochrometer was inserted before the incident beam. The peak broadening caused by the instrument was corrected with the use of Standard Reference Material (SRM) of Si (SRM 640d) provided by the National Institute of Standards and Technology (NIST). The measured peak broadening yields the crystallite size and microstrain following the Halder-Wagner method [5,6]:

$$\left(\frac{\beta^*}{d^*}\right)^2 = \frac{\beta^*}{D\ (d^*)^2} + (2\varepsilon)^2 \quad (1)$$

where β represents the full width at half maximum, giving $\beta^* = \beta \cos\theta / \lambda$, while λ denotes the wavelength of Cu Kα1, i.e. 1.5406 Å, D (the crystallite size), ε (microstrain), and $d^* = 2\theta / \lambda$ (the reciprocal of the lattice spacing), respectively. The crystallite size and strain was determined from the intercept and the slope of the linear plot of $(\beta^*/d^*)^2$ versus $\beta^*/(d^*)^2$.

3.3 Results and discussions

3.3.1 Shear strength of Ag pastes and their necking size

The shear strength of the Ag sinter die-attach joining is presented in Fig. 3.2, indicating that the bond strengths of S and F pastes exhibited about 30 MPa and 45 MPa, respectively. The cross-sectional SEM images of Ag joints with S and F pastes are shown in Figs. 3.2b-e, which indicate that both types of paste made robust bonding microstructures corresponding to the high shear strength. Compared to the Ag joint sintered by S paste, that with F pastes achieved thicker necking resulting in a relatively larger pore size. Obtained from the SEM images, the average pore sizes in the Ag joint layer made of sintered S and F pastes are found to be 1.052 μm^2, and 5.576 μm^2, respectively. The latter case of coarse grains and large necking provide a reasonable explanation of the superior shear strength of F paste joints over that of the S paste.

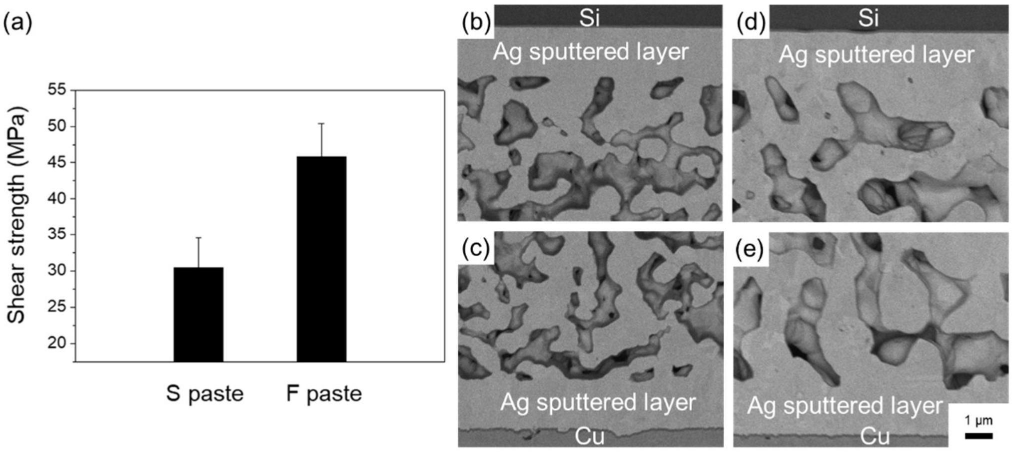

Fig 3.2. (a) Bonding shear strength of each sintered Ag joint. (b), (c) cross-section image of sintered joint of S paste at 250 °C for 1 hour. (d), (e) cross-section image of sintered joint of F paste at 250 °C for 1 hour.

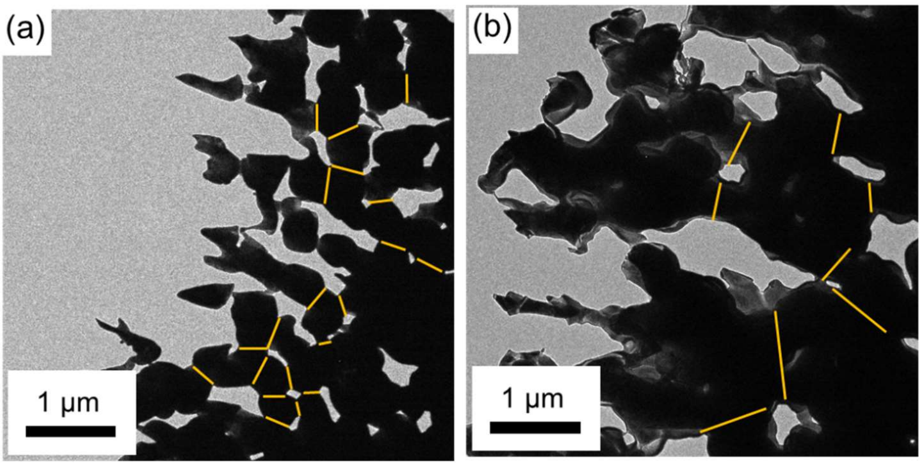

Fig. 3.3. TEM images of the pastes after sintering under air atmosphere at 250 °C for 10 min: S paste (a). F paste (b). Necking size is indicated by yellow line.

3.3.2 Microstructure observation of necking process with short time heating and *in situ* Ag nanoparticle formation

For a deeper understanding of the way the morphological evolution of bonding and, necking is realized in the two Ag pastes, TEM observations were conducted to observe the incipient Ag sintering process of the paste specimens at the initial stage of the heating process as shown in Fig. 3.3. Figs. 3.3 (a), (b) show low magnified TEM images of an Ag joint sintered with S paste and F paste, respectively, at 250 °C for 10 min. The necking size of the Ag joint is indicated by a yellow line. The average necking sizes of the Ag joint sintered using the S paste were smaller than those in the Ag joint sintered using F paste, as shown in Figs.3.3 (a), (b).

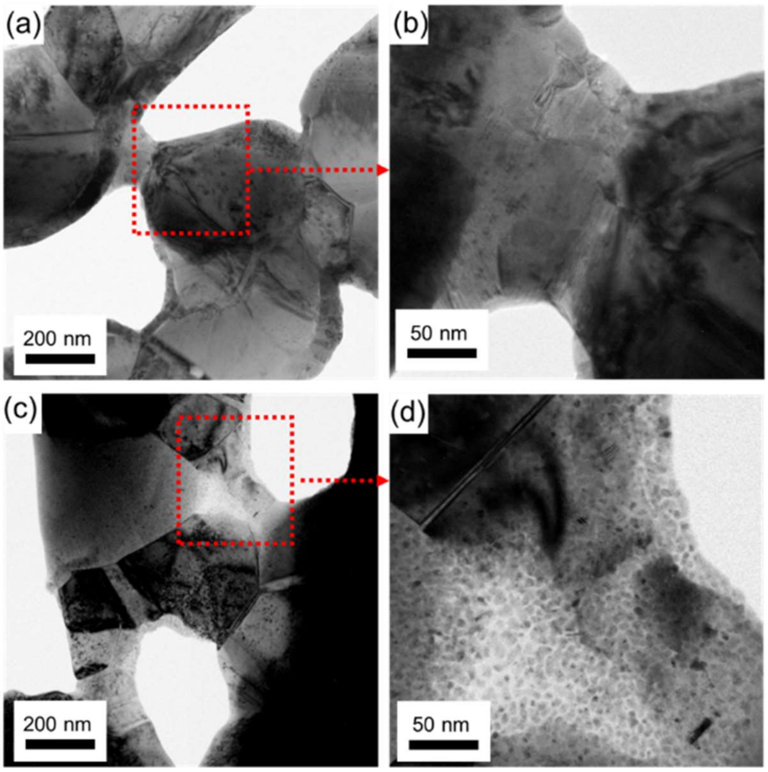

Fig 3.4. TEM images of the pastes after sintering under air atmosphere at 250 °C for 10 min: S paste (a), magnified view of S paste (b), F pastes (c), magnified view of F pastes (d).

The microstructure of sintering pastes in Figs. 3.4a-b obviously presents spreading networks among Ag necking. The necking formation of spherical particles is explained by particles surface diffusion: forming a contact area first, then necking is formed by mass transportation, thereby reducing the total surface energy from a positive curvature of spherical particles to a negative curvature of necking [7,8]. Though the theoretical rate of kinetic necking growth differ from the previously proposed model, generally higher curvature leads to faster sintering [7]. Despite the large flat surface of flake particle which is expected that their sintering kinetic should be slow, the average necking size of Ag flakes was thicker than that of sphere particles. These controversial results imply that the F paste has a unique sintering mechanism that cannot be explained by the conventional model of diffusional necking growth.

A unique phenomenon of F paste can be found in Fig. 3.4d where numerous Ag NPs are observed between large Ag particles, while no such nanoparticle is found in the starting materials prior to heating. Hence Ag NPs must have been produced during heating process of F paste. Since Ag NPs are thermodynamically unstable, agglomerating Ag NPs accelerate the networking among large Ag particles, contributing to the fast necking growth in F paste as shown in Fig. 3.4d.

The self-produced Ag NPs is inherent in the Ag flake particles used in F paste. It is widely known that such Ag NPs can be produced by the decomposition of Ag oxide at around 170 °C [5, 12, 13]. A reduction reaction in wet conditions is also believed another mechanism that assists in the formation of Ag NPs [12]. However, Ag flakes used in this study are pure Ag. Regardless of the presence of solvent, until 175 °C Ag flakes cannot form Ag NPs. Ag NPs are generated only when Ag flakes are sintered at 250 °C. This fact demonstrates that the self-production of Ag NPs is dependent upon heating temperature.

3.3.3 Previously reported Ag nanoparticles formation mechanism and microstrain in Ag particles

It has been reported that Ag NPs are formed by heating on cold-worked bulk Ag [13,14] and on sputtered Ag thin films deposited on a Si wafer [15], forming numbers of Ag hillocks. It is known that this Ag hillock growth is highly dependent on residual stress [16,17] and that the mechanism of hillock growth is governed by creep [16,17]. The previous study on Ag NPs formation follows residual stress introduced by the cold-worked process and of mechanical stress induced by CTE mismatch between Ag films and substrate in the latter case. Therefore, the one part of driving force of Ag NPs production is stress relaxation process. “Nano volcanic eruption theory” has been proposed to explain the relationship between self-produced Ag NPs and Ag hillock growth. This theory suggests that the oxidized Ag at grain boundaries transforms into a liquid phase by the reaction of oxygen and Ag at elevated temperature. Liquid Ag-O is emitted from pressurized grain boundaries and undergoes immediate decomposition into adatoms in air [15]. The phase transition to liquid of Ag-O occurs immediately at elevated temperature to crystallize the Ag NPs.

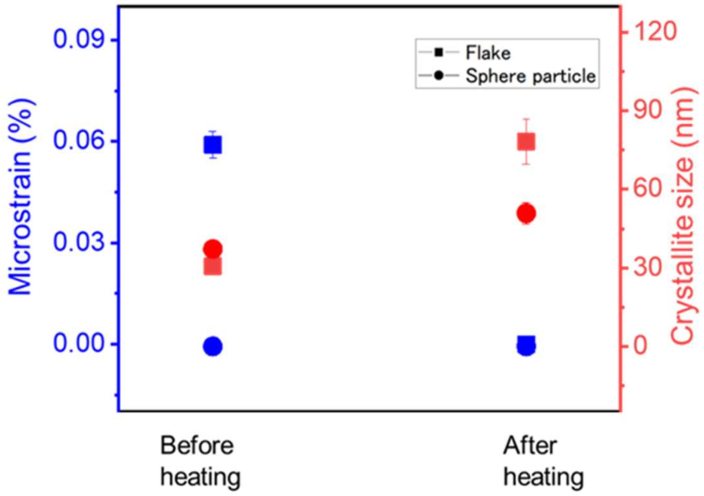

Fig 3.5 Evolution of microstrain and crystallite size evaluated by X-ray diffraction before and after heat treatment at 250 °C.

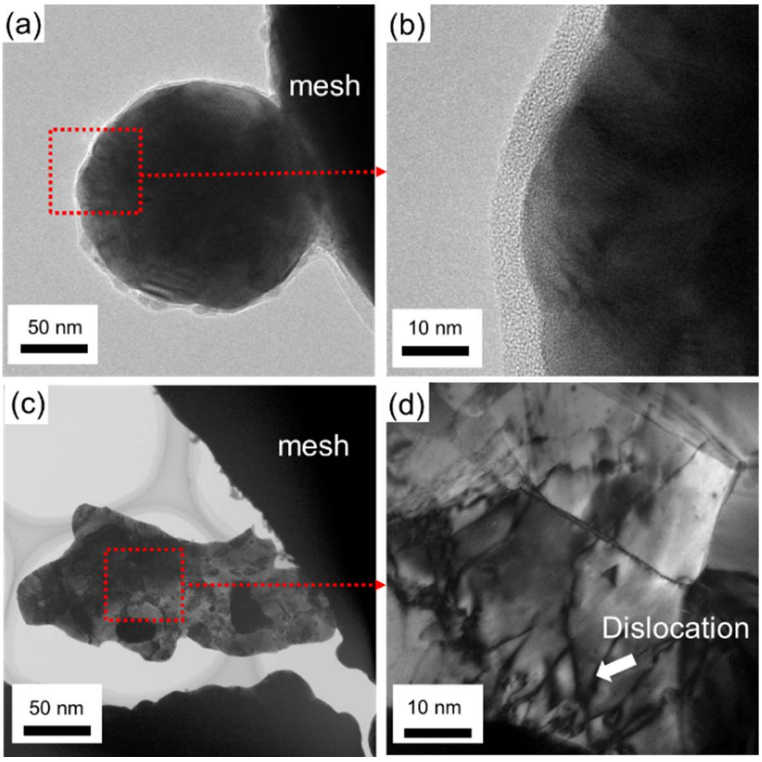

Fig 3.6 TEM images of initial Ag fillers; sphere particle (a), magnified view of sphere particle (b), Ag flake (c), magnified view of Ag flake (d).

The Halder-Wagner analysis of powder X-ray diffraction was used for quantitatively evaluation of internal stress in the original Ag particles. Depending on the methodology employed, for example, Williamson-Hall, the absolute value of crystallite size or microstrain may be different, however the overall trend remains unchanged (See supplementary materials.). The results presented in Fig. 3.5 reveal that the microstrain in the initial Ag flake reached about 0.06 %, while the spherical particles contained no strain at all. The average grain size of these initial particles was about 30 nm and 40 nm respectively. After the heating process, the microstrain in flakes disappeared, coinciding with nanoparticle creation. This phenomenon appears identical to the nanoparticle production with stress relaxation as discussed in the previous paragraph. The average crystallite size of flake-shaped and spherical particles increased to approximately 80 nm and 50 nm, respectively after sintering (See Fig. 3.5). The fast grain growth of Ag flake particles is, therefore, caused by the self-produced Ag NPs accompanied with strain relaxation.

To verify the source of initial microstress found only in Ag flake particles, TEM observation was carried out on both flake and spherical particles (See Fig. 3.6). Both particles appear as polycrystalline microstructures (see Fig. 3.6a, and b). Grains of the flake particles shows highly concentrated dislocations that can induce strain fields within grains. The relationship of microstrain and dislocation is known to follow the equation: $\rho = \frac{2\sqrt{3}\varepsilon}{Db}$, where ρ is dislocation density and b is Burger's vector [18–21]. Moreover, such high dislocation structure disappeared after the sintering as shown in Fig. 3.4. Thus, these TEM observations, along with the results obtained by XRD analysis, clearly demonstrate that only flake particles contain large initial strain field in the grains.

3.4 Conclusion

In summary, the sintering mechanism of Ag flake particles was investigated and compared with those of spherical particles. The spherical particles exhibited necking process followed by the conventional diffusion process. Flake particles, however, generated massive Ag NPs during heating and these Ag NPs accelerated the sintering process. The shear strengths of the sintered joints of F paste reached 45 MPa of die-attach joints, obviously higher than 30 MPa of S paste. The cross-sectional microstructure of die-attach joints indicates that the difference in shear strength can be attributed to the larger necking size for F paste. The origin of Ag NPs can be attributed to the initial microstrain, which was confirmed by XRD, and the subsequent strain relaxation on heating. TEM observation also suggests that the microstrain is due to the high dislocation density in grains of flake particles. Thus, present study clarifies the difference in sintering mechanisms of Ag paste made from flake and spherical particles. These findings represent significant contributions to the industrial application of large Ag particle paste suitable for sintering die-attach, and as a replacement for Pb-based solders currently used in power device packaging.

References

[1] D. Wakuda, M. Hatamura, K. Suganuma, Novel method for room temperature sintering of Ag nanoparticle paste in air, Chem. Phys. Lett. 441 (2007) 305–308.

[2] D. Wakuda, K.S. Kim, K. Suganuma, Room temperature sintering of Ag nanoparticles by drying solvent, Scr. Mater. 59 (2008) 649–652.

[3] M.A. Asoro, D. Kovar, P.J. Ferreira, Effect of surface carbon coating on sintering of silver nanoparticles: in situ TEM observations, Chem. Commun. 50 (2014) 4835–4838.

[4] K. Suganuma, S. Sakamoto, N. Kagami, D. Wakuda, K.S. Kim, M. Nogi, Low-temperature low-pressure die attach with hybrid silver particle paste, Microelectron. Reliab. 52 (2012) 375–380.

[5] N.C. Halder, C.N.J. Wagner, Separation of particle size and lattice strain in integral breadth measurements, Acta Crystallogr. 20 (1966) 312–313.

[6] Y. Kodera, N. Yamasaki, T. Yamamoto, T. Kawasaki, M. Ohyanagi, Z.A. Munir, Hydrogen storage Mg_2Ni alloy produced by induction field activated combustion synthesis, J. Alloys Compd. 446–447 (2007) 138–141.

[7] F. Thümmler, W. Thomma, The sintering process, Metall. Rev. 12 (1967) 69–108.

[8] G.C. Kuczynski, Self-diffusion in Sintering of Metallie Partieles, JOM. 1 (1949) 169–178.

[9] T. Morita, Y. Yasuda, E. Ide, Y. Akada, A. Hirose, Bonding technique using micro-scaled silver-oxide particles for in-situ formation of silver nanoparticles,

Mater. Trans. 49 (2008) 2875–2880.

[10] F. Mu, Z. Zhao, G. Zou, H. Bai, A. Wu, L. Liu, D. Zhang, Y.N. Zhou, Mechanism of Low Temperature Sintering-Bonding through In-Situ Formation of Silver Nanoparticles Using Silver Oxide Microparticles, Mater. Trans. 54 (2013) 872–878.

[11] H. Zhang, Y. Gao, J. Jiu, K. Suganuma, In situ bridging effect of Ag_2O on pressureless and low-temperature sintering of micron-scale silver paste, J. Alloys Compd. 696 (2017) 123–129.

[12] R.D. Glover, J.M. Miller, J.E. Hutchison, Generation of metal nanoparticles from silver and copper objects: Nanoparticle dynamics on surfaces and potential sources of nanoparticles in the environment, ACS Nano. 5 (2011) 8950–8957.

[13] S. Noh, C. Choe, C. Chen, K. Suganuma, Heat-resistant die-attach with cold-rolled Ag sheet, Appl. Phys. Express. 11 (2018).

[14] C. Chen, S. Noh, H. Zhang, C. Choe, J. Jiu, S. Nagao, K. Suganuma, Bonding technology based on solid porous Ag for large area chips, Scr. Mater. 146 (2018) 123–127.

[15] S. Lin, S. Nagao, E. Yokoi, C. Oh, H. Zhang, Y. Liu, K. Suganuma, Nano-volcanic Eruption of Silver, Sci. Rep. (2016) 34769.

[16] C. Oh, S. Nagao, T. Kunimune, K. Suganuma, Pressureless wafer bonding by turning hillocks into abnormal grain growths in Ag films, Appl. Phys. Lett. 104 (2014) 3–7.

[17] S.K. Sharma, J. Spitz, Hillock formation, hole growth and agglomeration in thin

silver films, Thin Solid Films. 65 (1980) 339–350.

[18] G.K. Williamson, R.E. Smallman, III. Dislocation densities in some annealed and cold-worked metals from measurements on the X-ray Debye-Scherrer spectrum, Philos. Mag. 1 (1956) 34–46.

[19] G.K. Williamson, W.H. Hall, X-ray line broadening from filed aluminium and wolfram, Acta Metall. 1 (1953) 22–31.

[20] S. Ni, Y.B. Wang, X.Z. Liao, S.N. Alhajeri, H.Q. Li, Y.H. Zhao, E.J. Lavernia, S.P. Ringer, T.G. Langdon, Y.T. Zhu, Grain growth and dislocation density evolution in a nanocrystalline Ni-Fe alloy induced by high-pressure torsion, Scr. Mater. 64 (2011) 327–330.

[21] A. Roh, H.Y. Um, D. Kim, S. Nam, H.S. Kim, H. Choi, Influence of high-pressure torsion and hot rolling on the microstructure and mechanical properties of aluminum–fullerene composites, J. Mater. Sci. 52 (2017) 11988–12000.

Supplementary Materials

Microstructure evaluation by X-ray diffraction.

To obtain qualitative size and strain information about the microstructure prior to any detailed analysis, the Halder–Wagner (HW) and Williamson–Hall (WH) methods are sufficiently effective. Note that, according to Scherrer, the crystallite size (D) is related to the peak broadening of XRD as follows [1]:

$$\beta_{crystallite\ size} = \frac{0.9\lambda}{Dcos\theta} \tag{S1}$$

where λ is the radiation wavelength, θ is Bragg's angle, and $\beta_{crystallite\ size}$ is the full width at half maximum (FWHM) solely due to crystallite size. Stokes and Wilson reported that the strained crystallite reflection exhibits peak broadening, which can be expressed by the following equation [2]:

$$\beta_{strain} = 4\epsilon \cdot \tan\theta \tag{S2}$$

where ϵ is the microstrain and β_{strain} is the FWHM solely due to strain. The HW assumption that the Lorentzian and Gaussian components of peak broadening are caused by size and strain, respectively, leads to the following equation [2–4]:

$$\left(\frac{\beta_{crytalite\ size}}{\beta_{total}}\right) = 1 - \left(\frac{\beta_{strain}}{\beta_{total}}\right)^2 \tag{S3}$$

Substituting equations (1) and (2) gives:

$$\left(\frac{\beta_{total}}{tan\theta}\right)^2 = \frac{0.9\lambda}{D}\frac{\beta_{total}}{tan\theta\sin\theta} + 16\epsilon^2 \tag{S4}$$

The WH method assumes that the broadening effect due to both size and strain is solely Lorentzian, which is expressed as follows [2,5,6]:

$$\beta_{total} = \beta_{crytalite\ size} + \beta_{strain} = \frac{0.9\lambda}{Dcos} + 4\epsilon\tan\theta \tag{S5}$$

The broadening effect of the Bragg peak comes from a combination of both instrumental and microstructural effects. To decompose the instrumental and microstructural peak broadening, a peak from a standard material that has a large crystallite size and no strain, can be assumed to represent a pure instrumental effect. In our research, the peak broadening caused by the instrument is corrected with the use of a Standard Reference Material (SRM) of Si (SRM 640d) provided by the National Institute of Standards and Technology (NIST). The instrument-corrected broadening was estimated using the equation [7,8]:

$$\beta_{microstructural\ effect}{}^{2} = \beta_{measured}{}^{2} - \beta_{instrumental}{}^{2} \qquad \text{(S6)}$$

XRD patterns of the samples are shown in Fig. S3.1 (a) and their normalized intensity in the 311 reflection are presented in Fig. S3.1 (b). The narrow breadth of the peaks indicates high crystallinity. Therefore, the flakes have low crystallinity compared to the spheres. After sintering, it is believed that high crystallinity is achieved and the flakes attain higher crystallinity than the spheres. The results were analyzed using the HW and WH methods. The corresponding plots are shown in Figs. S3.2 and S3.3, respectively. The HW and WH line plots were obtained from linear regression. The crystallite size and microstrain of the samples were obtained from the slope and intercept computed using equations (S4) and (S5). The crystallite size and microstrain with HW, WH, and Scherrer's methods are summarized in Table S3. While the obtained results are different, the trends in both microstrain and crystallite size do not change: the initial flake has a smaller size and a larger microstrain compared to the sphere, whereas after heating, all samples showed increased crystallite size and decreased microstrain.

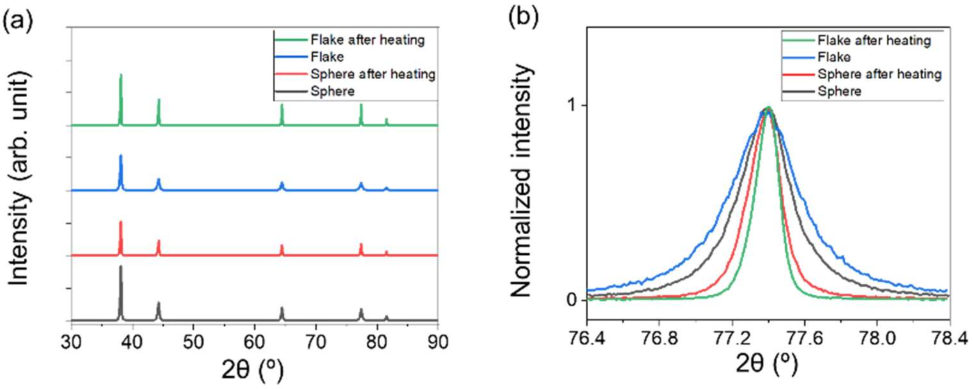

Fig. S3.1 (a) XRD patterns of Ag samples, and (b) normalized intensities at 311 reflection.

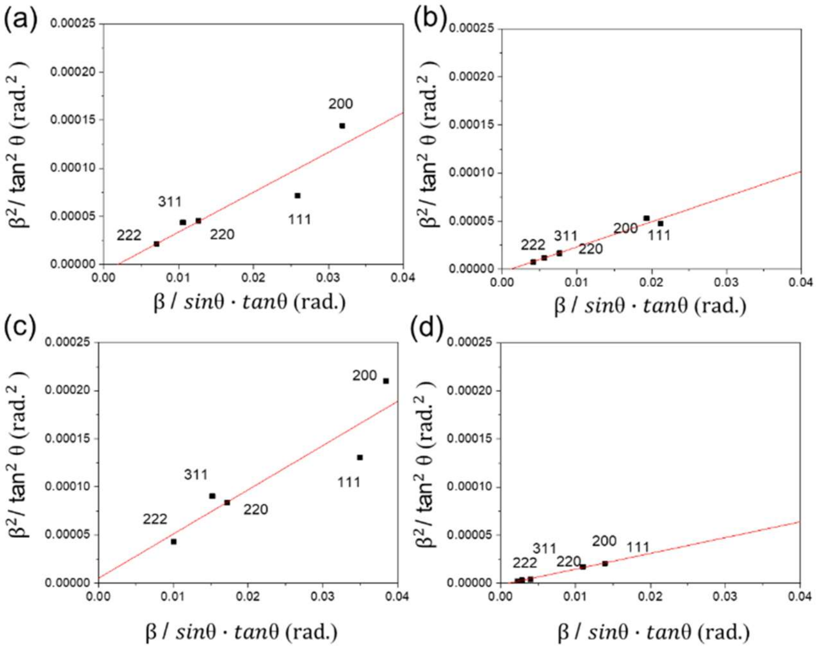

Fig. S3.2 Halder-Wagner plots of the samples: (a) sphere, (b) sphere after heating, (c) flake, (d) flake after heating.

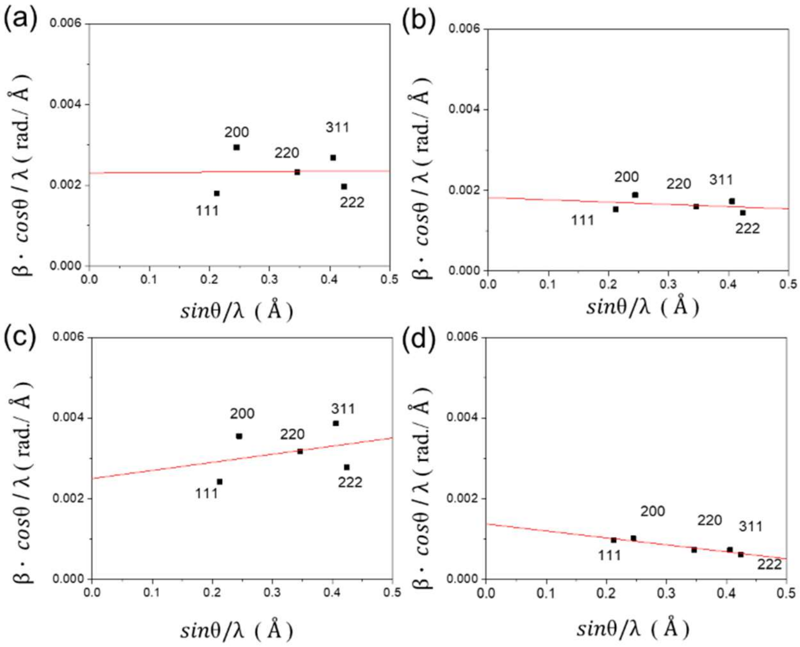

Fig. S3.3 Williamson–Hall plots of the samples: (a) sphere, (b) sphere after heating, (c) flake, (d) flake after heating.

Table S3 Average crystallite size D (nm) and microstrain ε (%) of the samples evaluated by XRD with HW, WH, and Scherrer's methods. The crystallite size of the samples obtained using Scherrer's method was evaluated by averaging the crystallite sizes obtained for all peaks. Numbers in brackets denote the standard deviation of the measurements.

	HW's method		WH's method		Scherrer's method
	D (nm)	ε (%)	D (nm)	ε (%)	D (nm)
Flake	30.7 (0.8)	0.059 (0.004)	38.2 (3.1)	0.051 (0.002)	27.1 (0.8)
Flake after heating	78.3 (8.6)	0	60.7 (6.8)	< 0	93.7 (12.0)
Sphere	37.2 (2.4)	0	42.5 (4.5)	0.011 (0.013)	35.8 (1.06)
Sphere after heating	50.9 (2.8)	0	46.7 (3.7)	< 0	55.4 (1.4)

References

[1] A. Khorsand Zak, W.H. Abd. Majid, M.E. Abrishami, R. Yousefi, X-ray analysis of ZnO nanoparticles by Williamson-Hall and size-strain plot methods, Solid State Sci. 13 (2011) 251–256.

[2] L. Motevalizadeh, Z. Heidary, M.E. Abrishami, Facile template-free hydrothermal synthesis and microstrain measurement of ZnO nanorods, Bull. Mater. Sci. 37 (2014) 397–405.

[3] N.C. Halder, C.N.J. Wagner, Separation of particle size and lattice strain in integral breadth measurements, Acta Crystallogr. 20 (1966) 312–313.

[4] Y. Kodera, N. Yamasaki, T. Yamamoto, T. Kawasaki, M. Ohyanagi, Z.A. Munir, Hydrogen storage Mg2Ni alloy produced by induction field activated combustion synthesis, J. Alloys Compd. 446–447 (2007) 138–141.

[5] T. Ungár, A. Borbély, The effect of dislocation contrast on x-ray line broadening: A new approach to line profile analysis, Appl. Phys. Lett. 69 (1996) 3173–3175.

[6] G.K. Williamson, W.H. Hall, X-ray line broadening from filed aluminium and wolfram, Acta Metall. 1 (1953) 22–31.

[7] A. Khorsand Zak, W.H. Abd. Majid, M.E. Abrishami, R. Yousefi, X-ray analysis of ZnO nanoparticles by Williamson-Hall and size-strain plot methods, Solid State Sci. 13 (2011) 251–256.

[8] J. Ghilane, F.R.F. Fan, A.J. Bard, N. Dunwoody, Facile electrochemical characterization of core/shell nanoparticles. Ag core/Ag2O shell structures, Nano Lett. 7 (2007) 1406–

1412.

Chapter 4

Sintering mechanism of micron Ag particles with polyol synthesis

4.1 Introduction

Chapter 3 dealt with low temperature sintering of Ag flake, however, the mechanism cannot apply to the sphere particles. To realize fast and low temperature mechanism of Ag paste, as is discussed from Chapter 2, *in-situ* polyol synthesis is introduced. Polyol synthesis is a wet process in high-boiling, multivalent alcohols to reduce dissolved metal cations. It is a cost effective and practical method compared to synthesis using reactive carbonyl metals or advanced organometallic compounds [1].

Micron Ag particles are cost-effective for use in the bonding process. However, to sinter micron Ag particles, a pressure condition of approximately 10–40 MPa is required [2–4]. Therefore, a pressure-less or low-pressure sintering process is required to avoid damage from the process and to enable the wide application of WBG devices. Hence, the direct use of micron Ag particles is not feasible based on the bonding process.

For a low-pressure bonding process, sintering of micron Ag is performed together with polyol synthesis, utilizing Ag nanoparticle formation or direct nucleation by a polyol process between the Ag microparticles. *In situ* polyol synthesis during sintering is introduced to prepare a new Ag paste composed of Ag fillers and a solution by mixing ethylene glycol (EG) and $AgNO_3$. The results showed that the sintered Ag tracks from the modified pastes exhibited a low resistivity at a low temperature. With polyol synthesis, the shear strengths of the Ag joint increased from 8.8, 9.2, and 6.8 MPa to 11.8, 15, and 13.0 MPa at 300 °C for the 1.5, 2, and 5 μm Ag particles, respectively. The effect of polyol synthesis on sintering is also discussed.

4.2 Experimental methods

4.2.1 Preparation of the Ag paste

Commercially available microscale Ag particles of three different sizes, with an average diameter of 1.5 μm, 2.5 μm, and 5 μm, were used (HWQ, Fukuda Metal Foil and Powder Co. Ltd) as the Ag fillers. The specific surface areas of the Ag particles were 1900, 2900, and 5500 cm^2 /g, respectively. Silver nitrate ($AgNO_3$) and EG ($C_2H_6O_2$, boiling point of 197 °C) were purchased from Wako Pure Chemical Industries Ltd. EG has a reducible effect and suitable viscosity; it is also effective for preparing Ag pastes. Ag pastes prepared by EG showed good electrical and bonding performance compared to those prepared by other solvents. In the first step, 5 g of $AgNO_3$ was added to 10 g of EG, and it dissolved and reacted under ultrasonication at 65 °C. The solution was used as a solvent for preparing the Ag paste. The Ag pastes were prepared by mixing the Ag fillers and solution or pure EG using a hybrid mixer (HM-500, Keyence, Osaka, Japan) for 5 min at a weight ratio of 5:1 or 10:1, as shown in Fig. 4.1(a). Ag pastes with and without $AgNO_3$ are referred to as modified Ag pastes and conventional Ag pastes, respectively. To ensure an applicable viscosity, a different weight ratio was used.

4.2.2 Sintering process

For the bonding process, Si dummy chips (3 mm × 3 mm × 0.5 mm) and Cu substrates (140 mm × 90 mm × 0.8 mm) were metalized with a 100 nm Ti layer by radiofrequency (RF) sputtering at a power of 100 W and a 2000 nm Ag layer by direct-current (DC) sputtering at 150 W. The pastes were printed on the substrates using a metal mask, and the Si dummy chip was placed on the printed pastes with a mild pressure of 0.4 MPa. Ag tracks (30 mm × 3 mm × 0.2 mm) were also printed on glass using a metal mask. First, the samples were heated to 130 °C for 25 min to promote a reduction reaction. During sintering, a hot plate was used with a heating rate of 25 °C/min. The samples were further heated to 200, 250, and 300 °C for 1 h. The detailed temperature profiles are shown in Fig. 4.1(b).

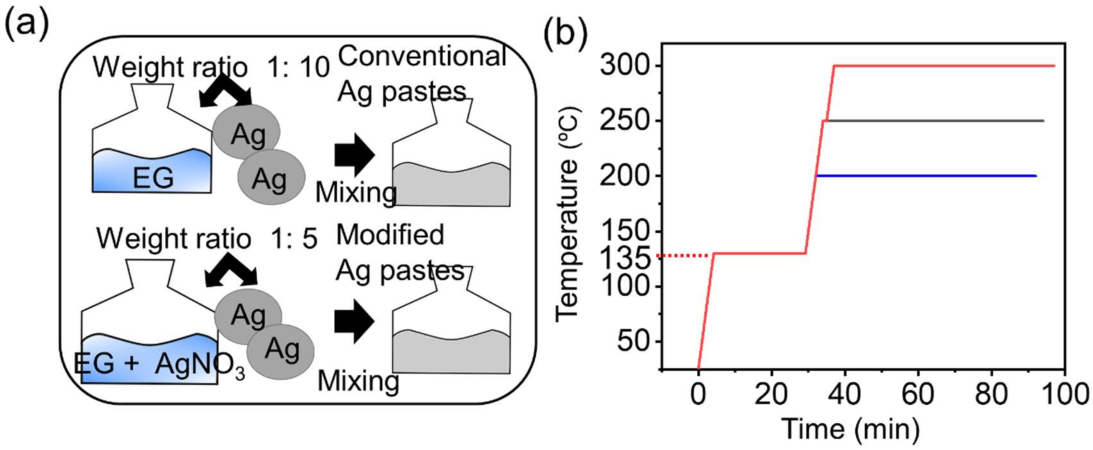

Fig. 4.1 Schematic illustration of the preparation of the (a) Ag pastes and (b) sintering profiles.

4.2.3 Characterization and evaluation of the Ag pastes and sintered structures

The thermal behavior of the Ag pastes was evaluated by a thermogravimetric (TG-DTA) analyzer (NETZSCH 2000SE) under an air atmosphere and a heating rate of 10 °C/min. X-ray diffraction (Rigaku RINT 2500) with Cu Ka radiation was used to evaluate the reduction process. A four-probe method was adopted to measure the electrical resistivity of the four samples of Ag tracks using a surface resistivity meter (Loresta GP T610, Mitsubishi Chemical Analytech Co. Ltd.). Five samples of the bonding joints were sheared to measure the shear strength using a die shear tester (Dage 4000) at a shear head speed of 50 μm/s. The morphology of the Ag particles and sintered structure were observed by SEM with an accelerating voltage of 5.0 kV.

4.3 Results and discussions

4.3.1 Evaluation of the modified pastes in a reduction process

Because $AgNO_3$ is expected to deteriorate the metallic bonding of the sintered Ag joint, the reaction should be optimized to achieve complete reduction or decomposition. Fig. 4.2 shows the TGA curves of the (a) conventional pastes and (b) modified pastes, heated to 450 °C under an air atmosphere. The weight change and thermal behavior of the Ag pastes exhibited the same trend regardless of the size of the Ag fillers. For all pastes, mass decrease and an endothermal peak were observed at approximately 130 °C, indicating evaporation or decomposition of the organics, which have a lower boiling point than EG. The mass decrease of all the pastes indicated that over 90% of the EG was decomposed or evaporated. The evaporation of the organics could be lowered owing to the catalytic activity of Ag [5]. The weight change and reaction of the conventional pastes and modified pastes were observed. The exothermal peak and mass decrease began at approximately 210 °C, and the mass decreased continuously below 350 °C for the new Ag pastes, as shown in Fig. 4.2(b). This could be from the reaction between the $AgNO_3$ and organics.

To further evaluate the reduction or decomposition reaction between the $AgNO_3$ and organics, TGA curves of $AgNO_3$ were obtained, as shown in Fig. 4.2(c). The endothermal reactions at approximately 170 °C and 210 °C were expected to occur due to the phase transition and melting of $AgNO_3$, respectively [6,7]. Because of the high rate of the liquid-liquid reaction, liquefaction of $AgNO_3$ should increase the rate of the decomposition reaction between the $AgNO_3$ and remnant organics. The results explained the sudden mass decrease of the new pastes. Further heating of $AgNO_3$ created two endothermal peaks at approximately 415 °C and 440 °C with a mass decrease, which represents the decomposition of $AgNO_3$ into oxygen and nitrogen dioxide [7]. Because the new pastes did not show a significant mass decrease near 440 °C, small amounts of remnant organics could effectively decompose $AgNO_3$, as shown in Fig. 4.2(b). Fig. 4.2(d) shows the XRD pattern of the new Ag pastes after sintering at 200 °C. The results showed that only a high-intensity peak of Ag was observed; therefore, a reduction or decomposition reaction was achieved, indicating that the bonding was metallic.

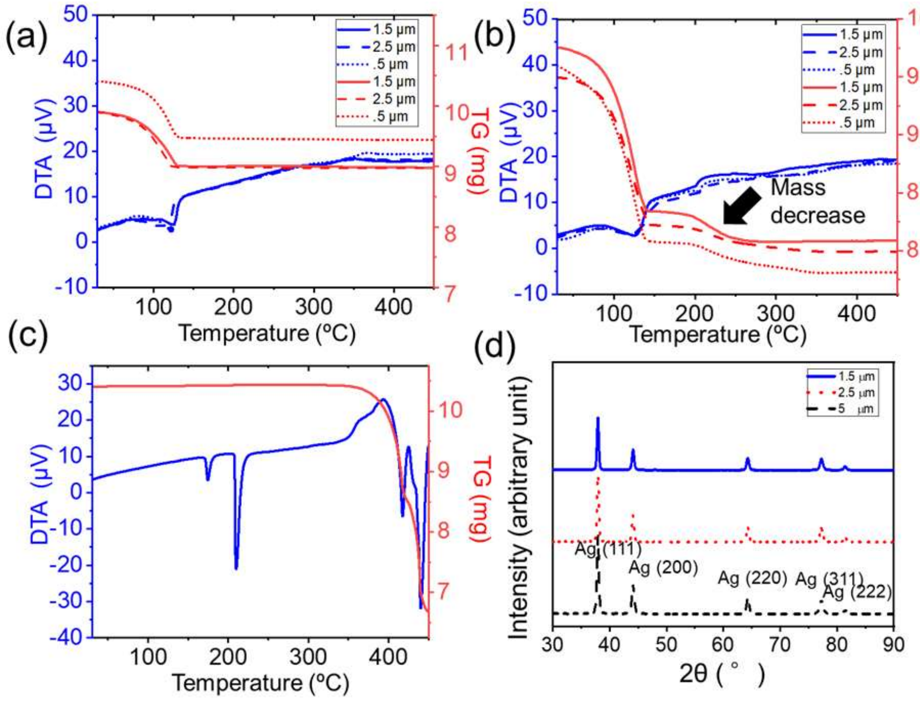

Fig. 4.2. TG-DTA results of (a) conventional Ag pastes, (b) Ag pastes with the polyol synthesis effect and (c) $AgNO_3$. (d) XRD pattern of the Ag pastes with polyol synthesis sintered at 200 °C and AgNO3. The length in the inset figure indicates the powder particle size.

4.3.2 Effect of in situ polyol synthesis on the sintering process

The electrical resistivity of the Ag tracks printed using the conventional and modified pastes is shown in Fig. 4.3. The electrical resistivity of the printed Ag tracks sintered at 200 and 250 °C could not be measured owing to fracture. The results suggested that the sintering of micron Ag pastes is difficult below 250 °C. However, the electrical resistivities of the Ag tracks decreased to approximately 17, 19, and 14 μΩ·cm at 300 °C for the 1.5, 2, and 5 μm Ag particles, respectively. The results indicated that the electrical resistivity was not directly related to the initial size of the Ag filler at the temperature; however, these results could be within the deviation range. Unlike the conventional pastes, the electrical resistivity of the modified pates could be measured below 250 °C; it reached 10^{-4} Ω·cm at 200 °C and decreased to approximately 36, 32, and 31 μΩ·cm at 250 °C and 17, 20, and 19 μΩ·cm at 300 °C for the 1.5, 2, and 5 μm Ag particles, respectively. The electrical resistivities of the Ag tracks using the new pastes were similar to those sintered by the conventional Ag pastes at 300 °C; however, the effect of polyol synthesis on sintering was marked at 250 °C, where the electrical resistivity of the Ag tracks distinctly decreased.

The surface SEM images of the Ag tracks sintered by conventional pastes are shown in Fig. 4.3. Necking between the Ag particles nearly did not occur, and a powderlike morphology was maintained at 200 and 250 °C, regardless of the size of the Ag fillers. The results corresponded well to the tendency of the electrical resistivity of the Ag tracks. Necking growth and coalescence were observed from the Ag tracks at 300 °C, as shown in Figs. 4.3(c, f, and i). However, the initial spherical morphology was maintained, indicating that the sintering was not complete at 300 °C owing to the large particle sizes.

The surface SEM images of the Ag tracks sintered by modified pastes are shown in Fig. 4.4. At 200 °C, a membrane-like morphology between the Ag particles was observed. The membrane-like morphology could be due to the reduction or decomposition reactions of $AgNO_3$ through in situ Ag nanoparticle formation and sintering or homogeneous nucleation. However, substantial coalescence of the Ag particles was not achieved below 200 °C. At 250 °C, faceted Ag surfaces were formed. The faceted Ag surface is generally observed during polyol synthesis, and the synthesized Ag particles have low indexed surfaces, such as (100) and (111) of the fcc structure to decrease the surface free energy. The relationship between the surface free energy and surface index is explained by the Wulff construction. The driving force to form faceted Ag surfaces is the surface energy difference between the sharp faceted Ag surface and membrane-like surface to create a locally stable structure. At 300 °C, the locally stable faceted Ag surfaces disappeared.

Compared to the conventional pastes, the modified pastes enabled substantial coalescence of the Ag particles and necking growth. The initial sphere structure was transformed into an Ag microporous skeleton structure with the progress of coalescence and thicker necking. The accelerated coalescence of the Ag particles was owing to a diffusion pathway, which connects the micron Ag particles. Without a diffusion pathway, as in the sintering of the conventional Ag particles, the contact area between the Ag particles started to undergo necking growth via a diffusion process. However, with the modified Ag pastes, at the initial stage of sintering, the contact area was formed by the chemical reaction and should be primarily responsible for accelerating the diffusion by connecting the particles.

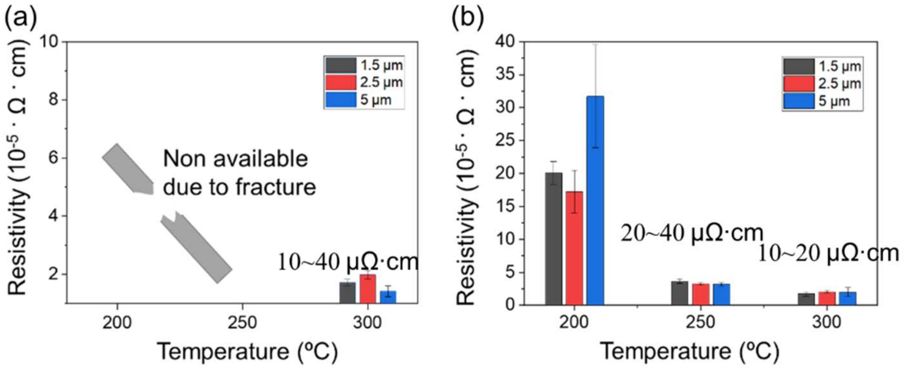

Fig. 4.3. Electrical resistivity of the Ag tracks printed using (a) the conventional pastes, (b) the modified pastes. The length in the figure indicates the initial Ag filler size.

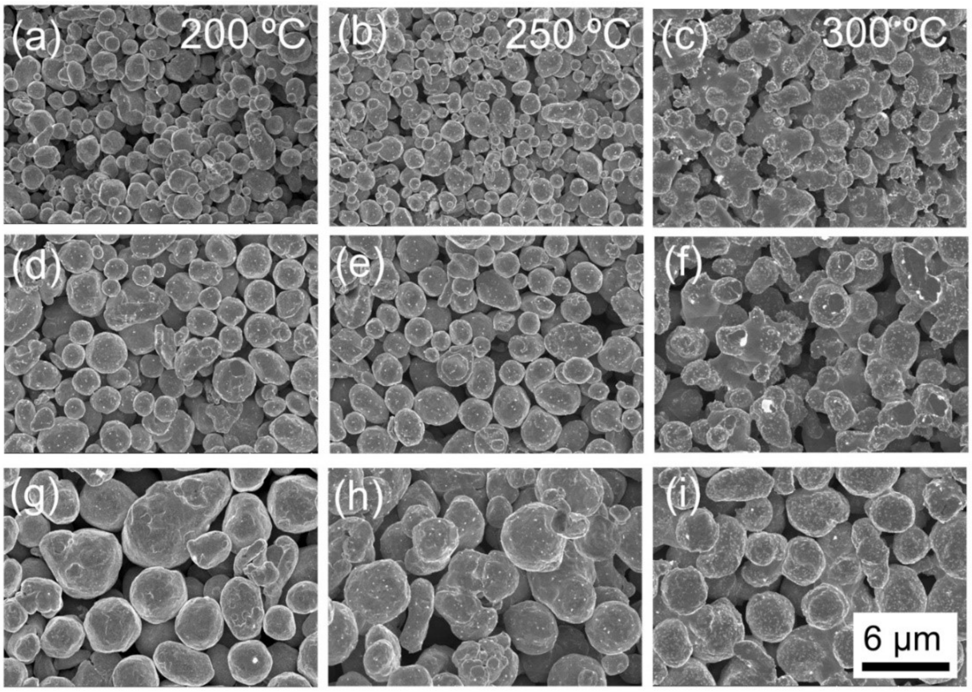

Fig. 4.4. Surface image of the sintered Ag tracks printed using the conventional pastes with Ag fillers of various sizes: (a)–(c) 1.5 μm, (d)–(f) 2.5 μm, and (g)–(i) 5.5 μm at (a,d,g) 200 °C, (b,e,f) 250 °C, and (c,f,i) 300 °C.

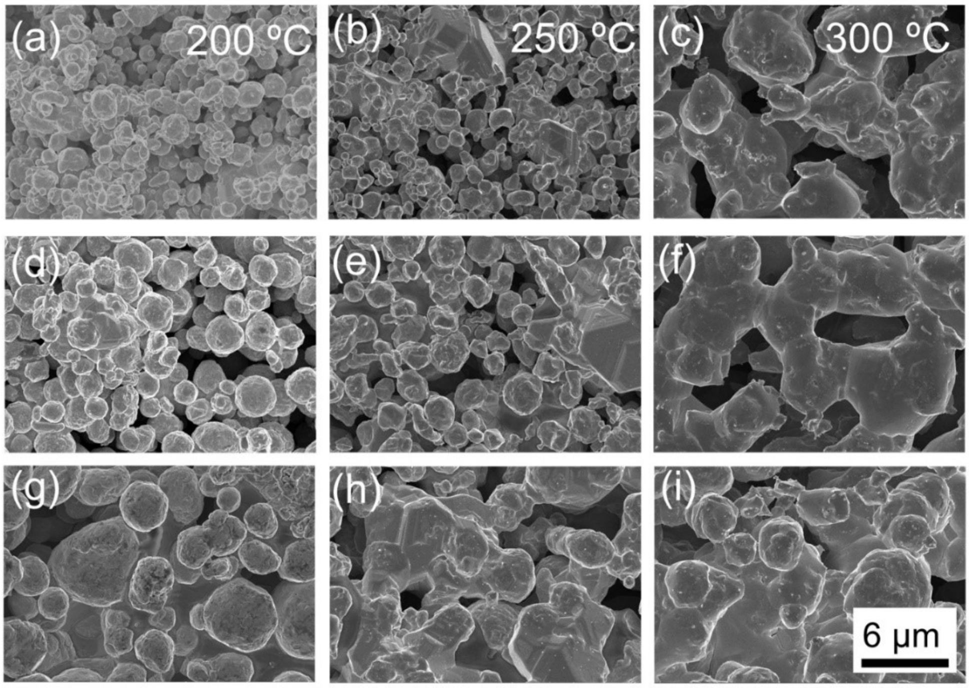

Fig. 4.5. Surface image of the sintered Ag tracks printed using the modified pastes with Ag fillers of various sizes: (a)–(c) 1.5 µm, (d)–(f) 2.5 µm, and (g)–(i) 5.5 µm at 200 °C (a,d,g), 250 °C (b,e,f), and 300 °C(c,f,i).

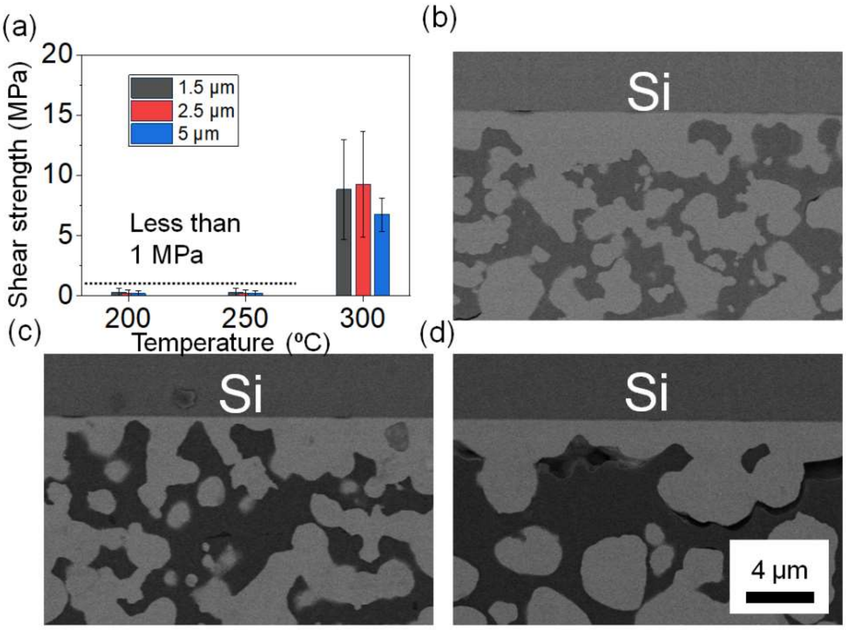

Fig. 4.6. Shear strength of the Ag joints sintered using the conventional pastes at (a) 200, 250, and 300 °C and cross-sectional images of the Ag joints from the pastes with filler of various sizes: (b) 1.5 µm, (c) 2.5 µm, and (d) 5.5 µm at 300 °C.

Fig. 4.6(a) shows the shear strength of the Ag joint achieved using conventional Ag pastes at 200, 250, and 300 °C. Regardless of the size difference among the Ag fillers, the conventional pastes failed to achieve stable bonding below 250 °C and showed a shear strength < 1 MPa. At 300 °C, the die shear strengths increased to 8.8, 9.2, and 6.8 MPa, and initial necking growth started from the microstructure, as shown in Figs. 4.6(b)–(d).

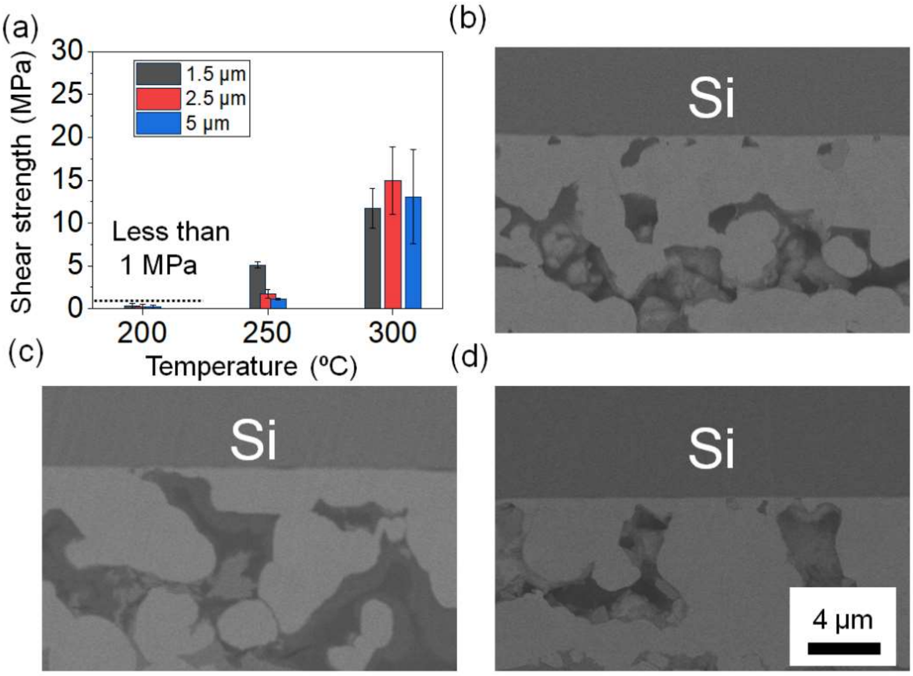

Fig. 4.7. Shear strength of the Ag joints sintered using the modified pastes at (a) 200, 250, and 300 °C and cross-sectional images of the Ag joint using the initial Ag filler size: (b) 1.5 μm, (c) 2.5 μm, and (d) 5.5 μm at 300 °C.

Fig. 4.7(a) shows the shear strength of the Ag joint achieved using modified Ag pastes at 200, 250, and 300 °C. The shear strength of the Ag joint was < 1 MPa at 200 °C; 5.0, 1.7, and 1.2 MPa at 250 °C; and 11.8, 15, and 13.0 MPa at 300 °C in the order of the Ag filler sizes. The membrane-like and faceted Ag surface should not contribute to the high shear strength. Although all cases showed an increased shear strength, the paste with the largest filler size, 5 μm, exhibited an approximately doubled shear strength. The microstructure of the interface of the Ag joint at 300 °C is shown in Figs. 4.7(b)–(d). Compared to the sintered Ag joint using conventional pastes, the sintered Ag joints using the modified paste showed a progressed coalescence structure and large necking. The results corresponded well with the increased shear strength.

4.4 Conclusion

The electrical and mechanical properties of micron Ag paste were improved by polyol synthesis. The Ag joints were structurally sound by sintering at 300 °C. The shear strengths of the Ag joints increased from 8.8, 9.2, and 6.8 MPa to 11.8, 15, and 13.0 MPa at 300 °C in the order of Ag filler sizes via polyol synthesis. The sintered Ag structure using the new Ag pastes showed thicker necking and substantial coalescence, compared to the sintered Ag structure using the conventional Ag pastes. The enhanced sintering performance could be because the new Ag pastes provided connected morphologies between the Ag particles via polyol synthesis, contributing to increased diffusion pathways.

References

[1] H. Dong, Y.-C. Chen, C. Feldmann, Polyol synthesis of nanoparticles: status and options regarding metals, oxides, chalcogenides, and non-metal elements, Green Chem. 17 (2015) 4107–4132.

[2] H. Zhang, Y. Gao, J. Jiu, K. Suganuma, In situ bridging effect of Ag 2 O on pressureless and low-temperature sintering of micron-scale silver paste, J. Alloys J. Compd. 696 (2017) 123–129.

[3] H. Schwarzbauer, R. Kuhnert, Novel large area joining technique for improved power device performance, IEEE Trans. Ind. Appl, 1991, pp. 93–95.

[4] K.S. Siow, Mechanical properties of nano-silver joints as die attach materials, J. Alloys Compd. 514 (2012) 6–19.

[5] J. Jiu, H. Zhang, S. Nagao, T. Sugahara, N. Kagami, Y. Suzuki, Y. Akai, K. Suganuma, Die-attaching silver paste based on a novel solvent for high-power semiconductor devices, J. Mater. Sci. 51 (2016) 3422–3430.

[6] F. Taylor, N. Ryde, N.S. Wales, Structural relationships between the polymorphs of silver nitrate, Acta Crystallogr. B 33 (1977) 311–313.

[7] A. Sobha, R.P. Aloysius, P. Guruswamy, K.G.K. Warrier, U. Syamaprasad, Phase evolution in Ag, Ag2O and AgNO3 added (Bi, Pb)-2223 superconductor, Physica C 307 (1998) 277–283.

This page is left blank intentionally.

Chapter 5

Conclusions

In this thesis, the interaction between chemically synthesized Ag particles and solvent, and developing in situ chemical synthesis sinter paste using redox reaction. The unique sintering mechanism of Ag flakes in situ formed Ag nanoparticles were presented.

In Chapter 1, the increase in demand for power devices and packaging, die-attach methods were summarized. The objectives of this study were also summarized: previously reported studies such as Ag flake and submicron hybrid paste or polyol-synthesized bimodal Ag pastes (micron and submicron) exhibited fast and sound bonding (~ 40 MPa) at low temperature less than 250 °C. Though above Ag pastes were composed of large size (micron and submicron) Ag particles, sintering is well achieved. The aim of this study was to understand low temperature sintering mechanism of above Ag pastes, and to develop advanced Ag sinter paste for realizing sound bonding which can endure severe operation conditions.

In Chapter 2, the sintering mechanism of "Polyol synthesized bimodal Ag paste (micron and submicron)" was investigated. During the sintering process, in situ formed Ag nanoparticles were observed only in Ag tracks derived from "polyol synthesized bimodal Ag paste" sintered at 175 °C, and they are considered to be the main driving force for particle sintering. The Ag nanoparticles are produced by the reduction of residual Ag ions by ethylene glycol, which can reduce metal ions to atoms. The electrical resistivity of the Ag wiring increased after the residual Ag ions were washed away from the polyol synthesized bimodal Ag particles. This result provided strong evidence for the hypothesis that the residual Ag ions can enhance the sintering of the Ag paste. The method described herein provides a new way to lower the sintering temperature and accelerate the sintering process without the need for using expensive Ag nanoparticles, and can be potentially applied in Ag sintering technology.

In Chapter 3, the sintering mechanism of Ag flake particles was investigated and compared with that of spherical particles. The spherical particles exhibited the necking process followed by conventional diffusion. The flake particles, however, generated Ag nanoparticles during the heating process, and these Ag nanoparticles accelerated the sintering process. The shear strength of the sintered joints using flake paste measured 45 MPa, obviously superior to 30 MPa achieved with the sphere paste. The cross-sectional microstructure indicates that the difference in shear strength can be attributed to the larger necking size, which is created by the Ag nanoparticles and the large contact area from the initial morphology. The origin of the Ag nanoparticles may be the initial microstrain identified by XRD and the subsequent strain relaxation on heating. TEM observations also suggest that the microstrain is caused by the high dislocation density in the grains of the flake particles. The present study has clarified the difference in the sintering mechanisms of Ag paste made from flakes and Ag paste made from spherical particles.

In Chapter 4, micron Ag paste were developed with polyol synthesis. Commercially available microscale Ag particles of three different sizes, with an average diameter of 1.5 μm, 2.5 μm, and 5 μm, were used (HWQ, Fukuda Metal Foil and Powder Co. Ltd) as the Ag fillers. 5 g of $AgNO_3$ was added to 10 g of EG, and it dissolved and reacted under ultrasonication at 65 °C. The solution was used as a solvent for preparing the Ag paste. The Ag pastes were prepared by mixing the Ag fillers and solution or pure ethylene glycol. The Ag joints were structurally sound by sintering at 300 °C. The shear strengths of the

Ag joints increased from 8.8, 9.2, and 6.8 MPa to 11.8, 15, and 13.0 MPa at 300 °C in the order of Ag filler sizes via polyol synthesis. The sintered Ag structure using the new Ag pastes showed thicker necking and substantial coalescence, compared to the sintered Ag structure using the conventional Ag pastes. The enhanced sintering performance could be because the new Ag pastes provided connected morphologies between the Ag particles via polyol synthesis, contributing to increased diffusion pathways.

The dissertation presented the unique factors of Ag sintering rather than the main driving force of sintering such as surface energy. The unique characteristic of synthesized Ag particle paste and micro-strained Ag particle paste exhibited in situ formation Ag NPs, without using organic additives for conservation. The mechanism and designing Ag pastes are believed to give ways realizing high temperature and high reliable packaging.

Research achievements

A. Papers

1. Jeyun Yeom, Shijo Nagao, Chuantong Chen, Tohru Sugahara, Hao Zhang, Chanyang Choe, Cai-Fu Li, and Katsuaki Suganuma, "Ag particles for sinter bonding: Flakes or spheres?" Applied Physics Letters, 114 (2019) 253103.
2. Jeyun Yeom, Zheng Zhang, Cai-Fu Li, and Katsuaki Suganuma, "Effect of polyol synthesis on sintering of microsized Ag particles" Microelectronics Reliability, 100–101 (2019) 113340.
3. Jeyun Yeom, Hao Zhang, Cai-Fu Li, Katsuaki Suganuma "Fast and low-temperature sintering of Ag paste due to nanoparticles formed in situ" Journal of Materials Science: Materials in Electronics, 30, 19, (2019), 18080–18087.
4. Seungjun Noh, Hao Zhang, Jeyun Yeom, Chuantong Chen, Cai-Fu Li, Katsuaki Suganuma "Large-area die-attachment by silver stress migration bonding for power device applications" Microelectronics Reliability, 88–90, (2018), 701-706.
5. Chuantong Chen, Jeyun Yeom, Chanyang Choe, Guiming Liu, Yue Gao, Zheng Zhang, Bowen Zhang, Dongjin Kim, Katsuaki Suganuma "Necking growth and mechanical properties of sintered Ag particles with different shapes under air and N2 atmosphere" Journal of Materials Science, 54, 20, (2019), 13344–13357.
6. Bowen Zhang, Chuantong Chen, Wanli Li, Jeyun Yeom, Katsuaki Suganuma, "Well - Controlled Decomposition of Copper Complex Inks Enabled by Metal Nanowire Networks for Highly Compact, Conductive, and Flexible Copper Films" Advanced Materials Interfaces, (2019), 1901550.

B. Proceeding and presentations

1. Jeyun Yeom, Cai-fu Li, and Katsuaki Suganuma, “Comparative study on sintering mechanism of bimodal silver particles paste” 2018 Annual Spring Meeting of The Japan Institute of Metal and Materials, Tokyo, Japan, March 20-22, 2018.
2. Jeyun Yeom, Cai-Fu Li, Katsuaki Suganuma, “Sintering mechanism of micron/submicron-size silver particles” 2018 International Conference on Electronics Packaging and iMAPS All Asia Conference (ICEP-IAAC), Kuwana, Japan, April 17–21 2018.
3. 廉　済胤、李　財富、菅沼　克昭、“銀マイクロフレークの焼結特性評価”エレクトロニクス実装学会秋季大会（MES2018)、 大阪大学吹田キャンパス、 2018 年 9 月 6 日-9 月 7 日
4. Jeyun Yeom, Cai-Fu Li, Katsuaki Suganuma, “Ag sintering with in-situ formation of nanoparticle: a sound Ag bonding technology for power electronics” The 20th International Symposium on Eco-Materials Processing and Design (ISEPD), Chungnam, Korea, January 4-7, 2019.
5. 廉　済胤、李　財富、菅沼　克昭、“マイクロ・サブマイクロサイズ銀粒子からの自己生成ナノ粒子による焼結メカニズム分析及びパワーエレクトロニクス実装”東京電機大学東京千住キャンパス, 2019 年 3 月 20 日-3 月 22 日
6. Jeyun Yeom, Zheng Zhang, Cai-Fu Li, and Katsuaki Suganuma, “Effect of polyol synthesis on sintering of microsized Ag particles” The 30th European Symposium on Reliability of Electron Devices, Failure Physics and Analysis (ESREF 2019), Toulouse, France, September 23-26.
7. Jeyun Yeom, Cai-Fu Li, Katsuaki Suganuma, “Modified micro-size Ag sinter paste for Wide Band Gap device packaging” The 2019 International Symposium on Advanced Power Packaging (ISAPP2019), Osaka, Japan, October 7-8.

Acknowledgment

I would like to express my sincere gratitude to my supervisor, Prof. Katsuaki Suganuma, for his support and academic guidance throughout my doctoral course. It was his steady support and inspiring guidance that brought this dissertation to its fruition. It was a great pleasure to conduct my work under his mentoring.

I would also like to appreciate members of doctoral committee, Prof. Yuichiro Koizumi, for insightful comments and helpful discussion for this dissertation.

I would so like to appreciate Assoc. Prof. Shijo Nagao and Assoc. Prof. Tohru Sugahara for their valuable advices and encouraging comments during preparation activities of this dissertation.

I am deeply grateful to Assoc. Prof. Cai-Fu Li, Dr. Jiu, Dr. Hao Zhang for their unlimited support on my publication activities.

I would like to express the appreciation to members and alumni of Suganuma Laboratory, Mr. Yukiharu Kimoto, Mr. Aishi Suetake, Dr. Wanli Li, Mr. Dongjin Kim, Ms. Bowen Zhang, Mr. Zheng Zhang, Ms. Sya, Ms. Keenan, Ms. Okuda, Ms. Moribe, Mr. Akio shimoyama, for their kind support.

Finally, I would like to express my sincere appreciation and love to my parents for their careful concern, moral support and dedication.

Jeyuun YEOM